

IMPERIAL

MENG INDIVIDUAL PROJECT

IMPERIAL COLLEGE LONDON

DEPARTMENT OF AERONAUTICS

Optimisation of 3D Printed Bone Screws

Author:
Imsara Samarasinghe

Supervisor:
Prof. Robert Hewson

Second Marker:
Dr. Roderick Lubbock

June 3, 2024

Abstract

Bone screws are a popular treatment method used in the field of orthopaedics to treat patients with bone fractures, or to correct deformities in bones and adjust posture. Bone screws and their designs have been available for decades, however, not much has changed in the way they are designed. Typically, studies on bone screws are experimental and doing so has led to a plethora of information on the effects of parameters such as pitch, major diameter and minor diameter on the pullout force of a bone screw. Varying these metrics does not seem to treat the problem of screw failure near the head of the screw, brought on by large shear stress concentrations formed during the pullout of the screw. This leads to the idea of using optimised structures and their benefits. Structures designed using topology optimisation for minimum compliance have already been created and used in many industries. Changing the optimisation problem to include stresses at boundaries allows the inner body of the screw to be designed such that the structure averages out the large shear stress concentrations across the entire outer boundary. Constraints are then added to ensure the screw body is capable of expanding under tensile loads. This prevents the screw from shrinking and failing during pullout. Variations of the final design are presented, to analyse the effectiveness of the structure to reduce shear stress concentrations and to highlight important parameters that affect the final material distribution created by solving the optimisation problem.

Acknowledgements

I would like to express my gratitude to my supervisor, Prof. Robert Hewson, for his encouragement and valuable expertise in multidisciplinary optimisation. I also thank Dr. Ryan Murphy for his help in setting up Firedrake and IPOPT. Finally, I am thankful to my family for their consistent support and encouragement throughout my academic career.

Contents

List of Figures	ii
List of Tables	iv
List of Symbols	v
1 Introduction	1
1.1 Introduction to bone and bone screws	1
1.2 Objectives	3
2 Literature Review	4
2.1 Bone Screws and their uses	4
2.2 Materials used in the manufacture of Bone Screws	5
2.3 Experimental optimisation of bone screws	7
2.4 Computational studies on bone screws	8
2.5 Introduction to topology optimisation	9
3 Methodology	10
3.1 Solid Isotropic Material with Penalisation (SIMP)	10
3.1.1 Problem Formulation	10
3.1.2 Density Filtering	11
3.1.3 Solving optimisation problems	13
3.1.4 Comparison of Solutions	14
3.2 Finite Elements for Linear Elasticity	15
3.3 Topology optimisation of bone screws	16
3.3.1 Problem setup	16
3.3.2 Objective function, J	17
3.3.3 Threshold Projection	18
3.3.4 Intermediate Density Penalisation	19
3.3.5 Auxeticity constraint	20
3.3.6 Displacement Constraint	21

3.3.7	Material deposition constraint	22
3.3.8	Final optimisation problem	23
4	Results and Discussion	25
4.1	Problems with asymmetry	25
4.2	Unoptimised stress distributions in a bone screw	26
4.3	Varying pullout force, P	27
4.4	Varying expansion forces, F	30
4.5	Varying a in the material deposition constraint	31
4.6	Evaluation of von Mises stresses, σ_M	33
4.7	Post-processing	34
5	Conclusion & future work	35
Bibliography		36

List of Figures

1.1	Spongy structure of Trabecular bone [3]	1
1.2	Fourth thoracic vertebra showing location of the Pedicle[3]	3
2.1	Types of bone screws	4
2.2	(a): Full contact between screw and bone; (b): loosening caused by stress shielding	5
2.3	Labelled Screw [4]	7
2.4	Variation of pullout resistance with screw parameters[4]	7
2.5	Auxetic Unit Cell with tunable parameters [32]	9
2.6	Leading edge droop nose rib [34, 35]	9
3.1	SIMP Interpolation scheme for different penalties	11
3.2	Solution to MBB beam with increasing mesh refinement [41]	12
3.3	Effect of Helmholtz filter on density distribution	12
3.4	Checkerboard effect in a cantilever beam	13
3.5	Flowchart describing the optimisation process	13
3.6	Comparison of solutions	15
3.7	finite element model for bone screw optimisation	16
3.8	Mesh convergence study	17
3.9	Fully grey design	18
3.10	Effect of beta on the linearity of the projection	19
3.11	Effect of projection filter on grey material ($\beta = 20$, $\eta = 0.5$)	19
3.12	Intermediate density penalisation with varying α	20
3.13	Formation of a single core structure in the design space	21
3.14	Square wave ($a = 15$) and its 2D projection onto the design domain Ω	22
3.15	Flowchart of optimisation process	24
4.1	Asymmetric material distribution with annotated line of symmetry	25
4.2	Expansion force histories	26
4.3	Evaluation of the shear stresses in an unoptimised screw body	27
4.4	Design and stress distribution for $P = 1000\text{N}$	27

4.5	Design and stress distribution for $P = 1500\text{N}$	28
4.6	Design and stress distribution for $P = 2000\text{N}$	28
4.7	Design and stress distribution for $P = 2500\text{N}$	28
4.8	Design and stress distribution for $P = 3000\text{N}$	29
4.9	The difference in shear stress peaks between the optimised and unoptimised screws	29
4.10	Design and stress distribution for $F = 300\text{N}$	30
4.11	Design and stress distribution for $F = 400\text{N}$	30
4.12	Design and stress distribution for $F = 400\text{N} P = 3000\text{N}$	30
4.13	Design and stress distribution for $a = 5$	31
4.14	Design and stress distribution for $a = 10$	32
4.15	Design and stress distribution for $a = 20$	32
4.16	Design and stress distribution for $a = 30$	32
4.17	Variation of peak shear stress with frequency, a	33
4.18	von Mises stress field for $P = 3000 \text{ N}$	33
4.19	Effect of post-processing on final material distributions	34

List of Tables

2.1	Metallic Alloy Material Properties [6, 17, 18, 20, 23]	6
3.1	Mesh properties	17
3.2	Titanium alloy properties	17
3.3	Optimisation parameters for promoting discrete designs	23
3.4	Constant simulation parameters for each sub-iteration	23
4.1	Constant simulation parameters	27

List of Symbols

SIMP	Solid Isotropic Material with Penalisation
PMMA	poly-methyl-methacrylate
PEEK	Polyether Ether Ketone
PLA	Polylactic Acid
PCL	Polycaprolactone
PLLA	Polylactic Acid
PGA	Polyglycolic Acid
STP	Stress Transfer Parameter
NPR	Negative Poissons Ratio
ESO	Evolutionary Structural Optimisation
LSM	Level Set Methods
Ω	Design domain
E_{max}	Young's modulus of given material
E_{min}	Small value representing the absence of material
ρ	Density distribution
p	Penalty for SIMP
V	Volume fraction
ν^0	Poisson ratio of given material
r	Helmholtz filter radius
$\tilde{\rho}$	Filtered densities from the Helmholtz filter
σ	Stress tensor
σ_{xx}	Stress parallel to x-axis
σ_{yy}	Stress parallel to y-axis
σ_{xy}	Shear stress
ε	Strain tensor
λ	Lamé parameter
μ	Iamé parameter
\mathbf{u}	Displacement vector
$\partial\Omega_D$	Dirichlet boundary such that $\partial\Omega_D \subset \Omega$
$\partial\Omega_N$	Neumann boundary such that $\partial\Omega_N \subset \Omega$
J	Objective function
$\bar{\sigma}_{xy}$	Average shear stress
β	Threshold projection parameter
η	Threshold projection parameter
$\tilde{\rho}$	Projected densities
α	Intermediate density penalty parameter
ϕ	measure of intermediate densities a design domain
ϕ_{max}	maximum allowed quantity of intermediate densities
LB	Lower bound
UB	Upper bound

Chapter 1

Introduction

1.1 Introduction to bone and bone screws

The adult human body contains a total of 213 bones [1]. The four general categories include long bones, short bones, flat bones, and irregular bones. The skeleton serves a multitude of functions for the human body. It allows for movement and locomotion by acting as a lever for muscles. It also protects internal organs [2]. Long bones typically comprise a tube-like structure known as the diaphysis and cone-shaped metaphyses below the diaphysis. [2, 3]. The diaphysis primarily comprises dense cortical bone, while the metaphysis is composed of trabecular bone [2]. Cortical bone is denser and more solid than trabecular bone, also known as cancellous bone, which has a spongy structure.

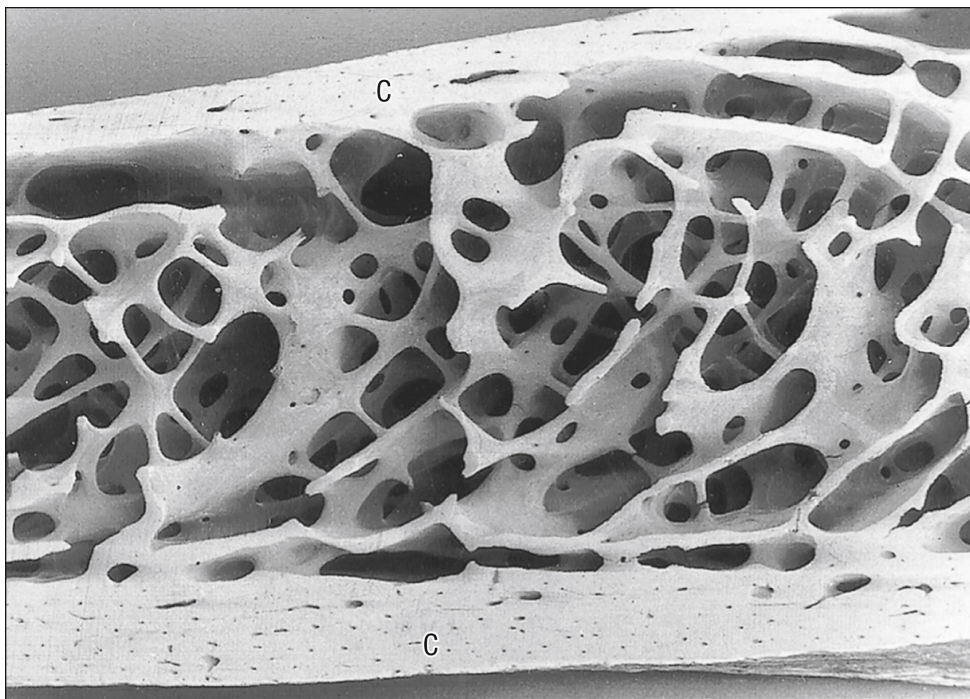


Figure 1.1: Spongy structure of Trabecular bone [3]

Fig. 1.1 shows the inner layout of the spongy tissue that forms the trabecular bone. This structure can support the cortical bone while lowering the weight of the bone itself. The two types of bone are also known to have complementary properties. Thick cortical bone is essential in resisting bending moments, while the trabecular bone can provide support in compression [3]. Bone is also known to be anisotropic.

Bone is a living tissue, capable of growth and self-repair, provided with the correct conditions and treatments.

Bone screws are common orthopaedic devices used in fracture fixation. Depending on factors such as fracture size, they are used alone or in conjunction with plates for better stabilisation [4]. They are also used to treat conditions caused by trauma and different forms of scoliosis [5]. In this case, pedicle screws are used in conjunction with spinal cages to correct deformities in the spine [4]. Bone screws, despite their heavy usage, have many flaws. Almost one-third of treated fractures using plates end in complications. 11% of these complications are screw related [6, 7]. These studies were performed on healthy individuals with non-osteoporotic bone. When bone screws are implanted in patients suffering from osteoporosis (loss of bone density), the failure rates may be higher than those predicted in the previous study [8]. It is well known that screw loosening rates in osteoporotic bone are much higher due to its inability to sustain high stresses [8, 9]. Studies conducted on non-osteoporotic patients indicate screw failure rates in the range of 1-15%, while the failure rates in osteoporotic patients are much higher and can go up to 60% [8, 10].

Complications are often caused by the stress-shielding effect of the metal screw body on the surrounding bone. Bone, as a living tissue, has the property to grow under stress and decay under the lack of stimuli. Bone screws are typically made of titanium alloys, with Young's moduli in the range of 100-200 GPa. Bone typically has a Young's modulus of 1-2 GPa. This large difference in stiffness leads to more of the usual stresses being carried through the screw body and not the bone itself. This causes decay around the screw body, leading to screw loosening and eventual implant failure [11]. This is the same effect that causes astronauts to lose bone mass in zero gravity, requiring them to take supplements and participate in regular exercise to maintain healthy bone mass. Loose screws are a danger to further microfracture of the bone and may pose a serious risk to patients, depending on the location of implantation [8, 11].

Another complication posed by bone screws is its holding power, otherwise known as the stripping strength of the screw. When a screw is loaded in tension, opposing forces will be generated in the bone in contact with the initial threaded section of the screw [11]. Due to the direction they are generated in, they are typically described as being shear stresses. The holding power of the screw will depend on the bone's ability to withstand these shear stresses during the tensile loading of a screw [11, 12]. Due to the difference in strengths of the screw material and the bone, failure will always occur on the bone side of the screw-bone interface [4]. This failure mechanism is typically quantified in the form of pullout tests of bone screws inserted into bone samples or pseudo-bone polyurethane blocks. The results of these studies are well known and have been used to design parameters of early screws, such as their pitch and diameters [4, 12]. The pullout resistance is ultimately dependent on the bone's resistance to shear loads, therefore the thread design of the screw is correlated to the pullout force [4, 11, 13]. The exact relationships will be elaborated further in the next chapter, but it is important to note that all studies found an increasing major diameter to be beneficial for resisting the shear loads. Unfortunately, simply changing the pitch and diameter of the screw does not create a suitable solution to this problem.

Fig. 1.2 shows the structure called the pedicle, which is part of the vertebra. Pedicle screws are severely limited by the space they have and optimisation based on the diameter is not possible. Therefore, other methods of reducing shear stress concentrations along the screw body must be explored. One such method is topology optimisation. This method can create structures given an objective function to minimise. In this study, the objective function would relate to the reduction of shear stress concentrations along the boundaries of the screw. It is an attractive method to solve this problem and has been utilised in aerospace and automotive settings to create optimised structures for various uses.

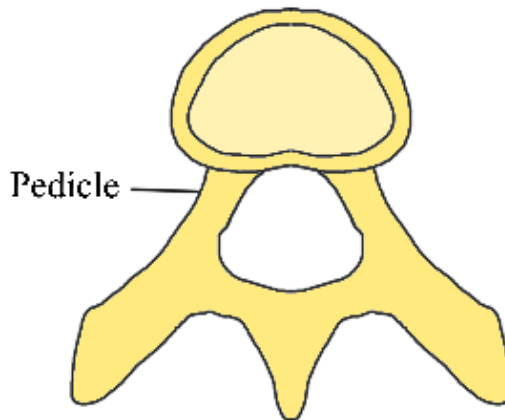


Figure 1.2: Fourth thoracic vertebra showing location of the Pedicle[3]

1.2 Objectives

Given the shortcomings of current bone screws and the lack of optimisation studies performed on bone screws using topology optimisation techniques, this project aims to:

1. Create and verify a baseline topology optimisation code which uses the solid isotropic material with penalisation (SIMP) technique
2. Modify the model to average shear stress concentrations across boundaries
3. Investigate negative Poissons ratio material distributions to produce expanding screw bodies.

These objectives create a clear plan to create an internal screw design using topology optimisation, capable of resisting shear loads and expanding within the bone to further increase its holding power.

Chapter 2

Literature Review

2.1 Bone Screws and their uses

Screw fixation methods for bone fractures have been available for more than 100 years. Bone screws were first introduced as a viable method for fixation in 1912 [6, 14]. Since then, the design has been improved through alterations in thread surface, and diameter, and the introduction of buttress threads. Material availability and improvements in manufacturing techniques eventually led to the use of titanium in the manufacture of bone screws [6, 15, 16]. In more recent times, bone screw optimisation has been carried out through means of changing screw geometry, threads, pitch, etc.

There are a variety of bone screws available on the market. Some screws are designed for treating only certain fracture types or fracture locations in the human body. A collection of these screws are provided in Fig. 2.1

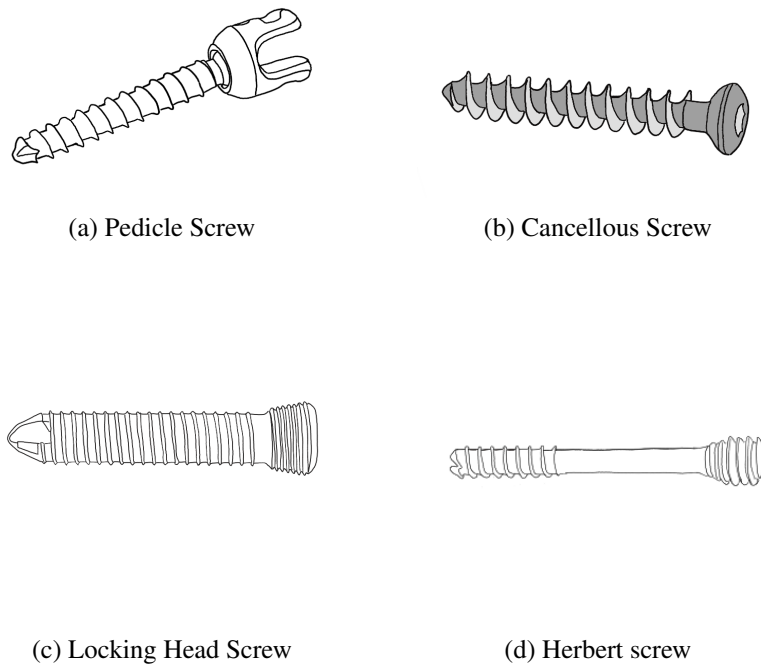


Figure 2.1: Types of bone screws

Fig. 2.1a depicts a pedicle screw. These screws are inserted into the pedicle of the vertebrae. The tops of these screws accommodate rods used for spinal cord alignment and stabilisation. These screws are used

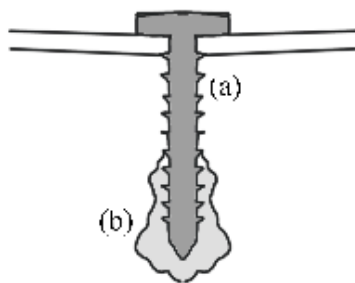


Figure 2.2: (a): Full contact between screw and bone; (b): loosening caused by stress shielding

in conjunction with cages for spinal correction or stabilisation in case of fracture or other conditions [9]. Fig. 2.1b depicts a cancellous screw. Note the large major diameter to minor diameter ratio that helps reduce the shear loading on the bone. Due to the softness of cancellous bone, these screws have to distribute shear loads more evenly. Fig. 2.1c presents a locking head screw. These screws are used in diaphyseal fractures [6]. Finally, Fig. 2.1d is the Herbert screw. These screws are typically small and are used for fracture fixation of small bones [6].

In chapter 1, the two main mechanisms of screw failure were discussed. The first mechanism is stress shielding and this occurs due to the stresses in bone being carried through the stiffer material of the screw. This leads to bone resorption around the screw and the process is illustrated in Fig. 2.2. Note the regions where the bone has decayed away from the implant, leading to the observed loosening of the bone screw.

The second mechanism is called screw retraction, otherwise known as screw pullout. These two mechanisms can lead to numerous failure modes. The most common mode due to stress shielding is screw loosening [6]. When it comes to the second mechanism, the failure mode is typically screw-purchase failure, where the interface between the screw and the bone fails due to high shear loads. There are many more complications such as screw cut-through, screw perforation and screw breakage due to high stresses at the fracture site[6]. These failure modes may be due to the combination of mechanisms detailed previously. This report will investigate the pullout mechanism, thereby its goal is to reduce the chance of failure of the screw-bone interface. The investigation will mainly focus on the shear forces and the impact these shear forces have on the bone surrounding the screw. The design of the novel topologically optimised screw is to reduce the shear stress concentrations that occur around the threads of the screw during pullout.

2.2 Materials used in the manufacture of Bone Screws

Metals are the most widely used material in the manufacture of bone screws. They have many advantages to their use. Metal bone screws provide high strength and high fracture toughness. Certain metals provide excellent biocompatibility [6, 17, 18]. The most commonly used metals are titanium, stainless steel, and cobalt alloys [6]. Titanium-based alloys used for implants have been reported to have excellent biological compatibility as well as being ductile [6, 19, 20]. Studies have investigated the biocompatibility of titanium alloys by testing its surface on implants in rabbits[6, 21]. When the implants were later harvested and tested they showcased higher bonding strength and higher bone contact. This shows that titanium alloys have excellent osseointegration properties. Another study aimed to use titanium alloys to 3D print screws with metamaterials [22]. These metamaterials were designed to improve the screw's performance in loosening. The results show that the auxetic structure of the screw was able to resist higher pullout forces than conventional screws. Another metal that is considered due to its properties is cobalt. These materials are considered due to their high strength and chemical resistance [6]. Tab. 2.1 shows the properties of conventionally used alloys in the manufacture of bone screws.

Table 2.1: Metallic Alloy Material Properties [6, 17, 18, 20, 23]

Alloy Name	Young's Modulus (GPa)	Elastic Modulus (GPa)	Yield Strength (MPa)	Ultimate Tensile Strength (MPa)
ASTM 316L Stainless steel	195-200	202	250	550
ASTM 22-13-5 Stainless steel	193-200	200	827	1069
Titanium Alloy Ti-6Al-4V	113	110-114	795-895	985
Cobalt Chrome F5262	230-240	220	950-1000	1200

Another interesting material being considered for use in the manufacture of bone screws is magnesium. Magnesium is an essential mineral that is required by the human body for promoting healthy bone growth. Magnesium alloys can provide good biocompatibility. These alloys can naturally degrade within the human body [6]. The magnesium is then absorbed by the body, which promotes further bone growth. Another advantage is the similarity in Young's modulus of magnesium alloys to bone [6]. This similarity is important as it would reduce the stress shielding effect of conventional screws discussed in the previous sections.

Apart from metals, polymers are also considered an important material in the production of bone screws and biomedical implants. Polymers such as poly-methyl-methacrylate (PMMA) have been used as bone cement and void fillers [6]. Some polymers such as polyether-ether-ketone (PEEK) have similar physical properties to bone and behave well under many medical procedures such as X-rays. They are also highly resistant to wear from chemicals [6]. Polymeric materials such as PLA, PCL, PLLA and PGA are used frequently in orthopaedics due to their biodegradability. Biodegradable screws offer the additional benefit of eliminating the need for revision surgeries to remove the screws. After healing occurs the bone can fully occupy the space from the screw getting rid of any stress peaks and any complications that may arise from stress shielding. An additional benefit of utilizing polymers in manufacturing is the accessibility of additive manufacturing techniques for creating porous screw geometries. For instance, research studies have explored the impact of 3D-printed porous polymeric screws on the osseointegration properties, as demonstrated in the work of Dhandapani *et al.* [24]. The study showed that the PLA screw, when immersed in body fluid showed the growth of osteoblast-like cells and the formation of calcium. Osteoblasts are cells involved in bone growth and are found as a layer over growing bone [25]. As of yet, only PLA and PCL polymers have been investigated for the additive manufacturing of bone screws. This project will focus on investigating the structure formed using titanium alloys, given their established effectiveness and excellent biocompatibility as demonstrated by previous studies. While polymer-based screws are innovative, their design is not within the scope of this report.

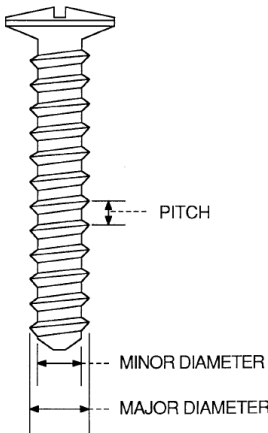


Figure 2.3: Labelled Screw [4]

2.3 Experimental optimisation of bone screws

The optimisation of bone screws has been thoroughly investigated through experimental methods. Due to the nature of these methods the optimisation process, or rather investigations of screw properties that impact pullout force, have been limited to the external features of the screw. The main external features of the screw are described in Fig. 2.3. The pitch of a screw indicates the distance between each thread. The major diameter refers to the diameter measured from the crests of the threads, while the minor diameter represents the diameter of the screw's body.

An important study in the investigation of screw features that affect the pullout force is the study by de Coster *et al.*[4]. As previously noted, the failure during pullout always occurs on the bone side of the screw-bone interface. The screw material is much stronger and can strip the threads in the bone. This study investigated the difficulty in measuring accurate bone pullout forces due to the large variation in cadaveric and animal bone samples. These variations primarily arise from factors such as specimen age and diseases like osteoporosis. Previous studies failed to establish a correlation between screw parameters and pullout force due to this variability. The chosen solution involved using a bone substitute in the form of polyurethane foam, with densities matched to that of bone by achieving an equivalent pullout force to that of a known screw type. The foam density is repeatable and reduces variation in the collected data. By drilling screws with different screw parameters into the "bone sample" and measuring its pullout force through a special rig, they were able to quantify the effect of screw design on its performance.

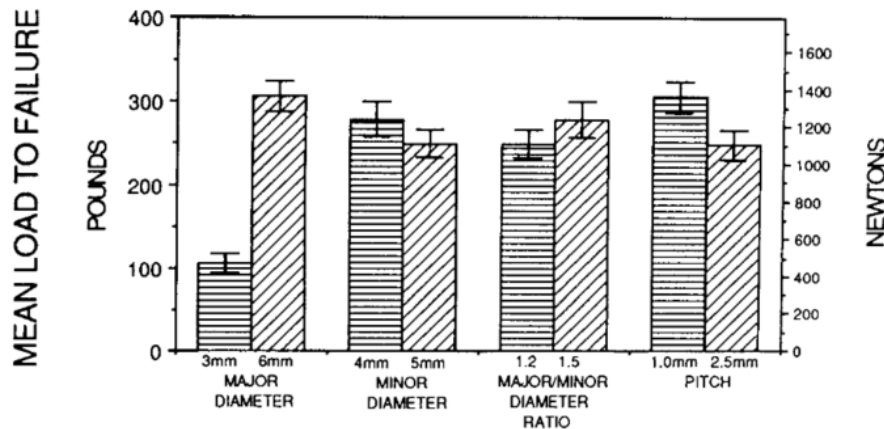


Figure 2.4: Variation of pullout resistance with screw parameters[4]

Fig. 2.4 shows the effect of screw design on the maximum pullout force of a screw, as measured by de Coster *et al.* It shows that increasing the major diameter increases the pullout force of a screw. An increasing minor diameter is associated with a decreased pullout force. Finally, a smaller pitch results in increased pullout resistance. It is also noted that increasing the major diameter is not a suitable method of increasing pullout resistance due to spacial constraints in certain bones. The study by Çetin *et al.* [26] investigated the effect of screw diameter and the effect of foam density on the pullout force of a screw. This study validates that increasing the major diameter directly correlates with an increase in the pullout force of a screw. The study also concludes that increasing foam density increases the pullout force of a screw. These results are corroborated by the collective findings of several other studies[27, 28]. Added complexity has been investigated by Gustafson *et al.* [13]. In this study pitch variation along a screw and tapered screws were investigated to find their pullout resistances. Their findings conclude that constant pitch screws had better pullout resistance compared to their variable counterparts. They also found that tapered screws had better pullout resistance compared to non-tapered screws. This effect may be due to the ability of tapered screws to tap into cleaner bone when being inserted, allowing for a stronger bond to be made. The final feature to be investigated is the shape of the thread itself. The studies referenced in [29, 30] both conclude that V-shaped or triangular threads tend to exhibit the highest pullout resistance. From the thread tested, s-shaped threads had the lowest pullout resistance [29]. These studies confirm that the maximum pullout force of a screw depends on the shear stress concentrations it produces on the surrounding bone. Variations in the pitch and major and minor diameter affect the volume of bone present in between the threads. When a greater amount of bone is present, higher shear loads can be withstood. Experimental studies have also been conducted to directly measure the locations of these shear concentrations using photoelastic models [31]. These models confirm the existence of shear stress concentrations and can locate them at the threads near the head of the screw. It is now evident that an optimised screw body should be capable of reducing these shear stress concentrations to prevent interface failure during pullout.

2.4 Computational studies on bone screws

Computational studies have also been performed to investigate screw parameters. One such study built finite element models of screws in bone [11]. The investigation is built on the premise that screws must be able to effectively transfer loads to surrounding bone to prevent bone resorption and stripping during pullout. To measure the effectiveness of screw design, this study creates a Stress Transfer Parameter (STP). Higher STP values indicate more effective screw designs. The study concluded that an increasing major diameter and number of threads increased the effectiveness of a screw, confirming the experimental studies in [4, 13, 26]. Furthermore, this study also investigated the effect of active-compression screws which expand post-insertion. The study concluded that this type of screw design had the highest STP overall. This finding gives the motivation to design more bone screws with the ability to expand *in vivo* and will be later explored through means of topology optimisation.

Metamaterials are specially designed materials, engineered to have a property that may not be present under natural conditions. Metamaterials are designed at the micro or nanoscale level to create materials that have unique properties. Most metamaterials consist of repeated unit cells with tunable parameters that will affect the material's overall properties. Fig. 2.5 shows a typical entrant cell with amendable parameters.

With tunable characteristics, metamaterials can produce materials with a negative Poissons ratio (NPR). Normally, when a material is stretched in one direction it shrinks in the orthogonal direction to the load. With NPR materials, expansion in orthogonal directions can be achieved. Previous studies showed the most effective screw type was a compression screw that was expanded *in vivo*[11]. If NPR screws were used, the same compressive effect could be achieved leading to higher pullout resistance. A study by Yao *et al.*[33] designed screws with auxetic unit cells and manufactured them using 3D printing. They then

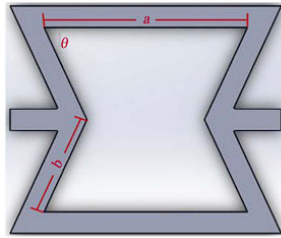


Figure 2.5: Auxetic Unit Cell with tunable parameters [32]

tested these models and found they performed better in pullout compared to conventional screw designs. It is now evident that expanding screw bodies are essential for enhancing the pullout performance of bone screws.

2.5 Introduction to topology optimisation

Topology Optimisation is a technique developed to create unique and heavily optimised structures to perform key tasks. These structures can be lightweight and perform well under their unique loading conditions. Optimised structures are typically created by the distribution of materials through a search space such that it satisfies boundary and loading conditions. It is a technique that has gained mainstream popularity in the aerospace and automotive industries due to the need for lightweight higher-performance structures. An example would be the leading edge droop nose rib design utilised in the Airbus A380, shown in Fig. 2.6. This design was created using topology optimisation to meet structural weight saving while keeping its performance [34, 35].

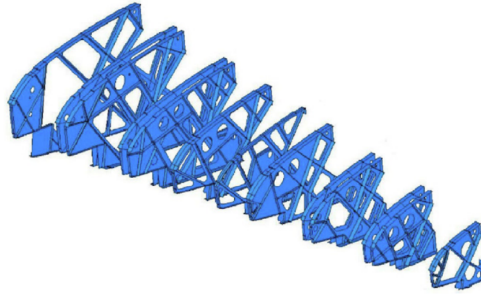


Figure 2.6: Leading edge droop nose rib [34, 35]

Topology optimisation can be investigated through several different algorithms, namely ESO, LSM and density-based methods. The ESO, or evolutionary structural optimisation, method utilises heuristic strategies to remove inefficient or unloaded material [34, 36]. This method does lead to some difficulties so a bi-directional version of the method was introduced. This new version could add material to regions with higher stresses[36]. The level set method(LSM) uses high dimensional level set functions to describe structural boundaries. The optimum configuration was then obtained through an iterative solution of the Hamilton-Jacobi equation[34]. On the other hand, density-based methods modelled the design domain through a discrete (0-1) density variable representing the distribution of material in the domain. These methods gained popularity with the introduction of the Solid Isotropic Material with Penalisation (SIMP) algorithm by Bendsøe and Kikuchi [37]. The SIMP methodology has been investigated thoroughly over the years and has been used in many use cases, from creating novel metamaterials [38, 39] to creating compliant mechanisms [40]. Its popularity, proven potential and availability of information makes SIMP the ideal choice for the investigation of novel screw structures.

Chapter 3

Methodology

3.1 Solid Isotropic Material with Penalisation (SIMP)

This section aims to introduce the SIMP methodology used for the creation of optimised bone screws. It also presents the creation of the base topology optimisation code and the verification of results from this base code.

3.1.1 Problem Formulation

In general, structural optimisation can consist of size, shape and topology optimisation. Size optimisation might consist of finding the ideal thickness distribution of a cantilever beam to meet certain conditions. A shape optimisation problem might change the shape of already existing structural elements to meet certain design criteria. On the other hand, topology optimisation requires the search for features such as the shape and location of holes within a domain [41]. In topology optimisation, the only known quantities are the boundary conditions and loads experienced by the design domain, Ω . In the first part of the report, the design will focus on developing a general topology optimization code using Firedrake for the well-known minimum compliance problem for verification purposes. To make such an optimisation problem it is important to visualise that the problem requires an optimum material distribution in the reference domain defined as, $\Omega \in \mathbb{R}^2$. Compliance is simply the inverse of stiffness, so the goal is to find the ideal stiffness tensor over the domain. Achieving this goal requires the allocation of a given material (or densities) in appropriate locations through the design domain, such that the objective function

$$J_{compliance} = \int_{\partial\Omega_N} t \cdot v dS \quad (3.1)$$

is minimised. To solve this problem the required discrete densities are modelled by continuous values that are penalised to drive the problem towards the original discrete values [41]. The most popular density-based method is the SIMP scheme. It has been developed in several open-source topology optimisation codes [42, 43] and the material interpolation used in this scheme is given as

$$E = E_{min} + (E_{max} - E_{min})\rho^p \quad (3.2)$$

In this setting ρ is the density/material distribution and represents the location of material in the design space. The penalty for driving the solution towards discrete values is referred to by p . The value E_{min} is typically set to a very small value and it is used to represent the absence of material at a location in the design space. E_{max} is set to the Young's modulus of the given material used for creating the design.

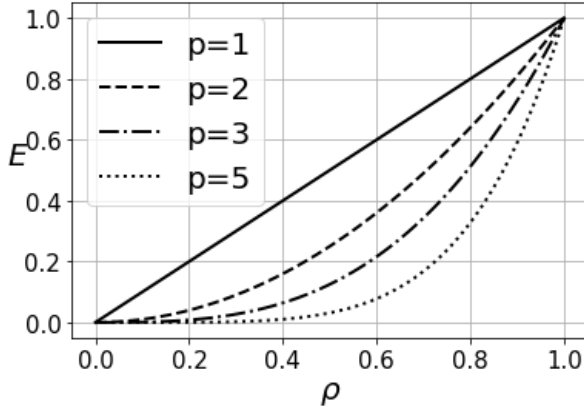


Figure 3.1: SIMP Interpolation scheme for different penalties

When $\rho \rightarrow 0$, $E \rightarrow E_{min}$ and is equivalent to no material at that location. When $\rho \rightarrow 1$, $E \rightarrow E_{max}$ and is equivalent to the given material present at this location. The interpolation scheme can now determine the presence of material in locations throughout the domain Ω , subject to the objective of the optimisation problem. Fig. 3.1 shows the effect of the different penalty values in driving the continuous value problem towards a discrete one.

The material penalty is typically chosen such that $p > 1$. This ensures that intermediate densities provide smaller stiffness, meaning that it is no longer economical to choose such a value given the cost of the material. This cost is governed by setting a volume constraint, written as

$$\int_{\Omega} \rho d\Omega \leq V \quad (3.3)$$

which governs the amount of material available for creating the optimised structure. The higher the penalty the lower the stiffness provided by intermediate densities, which can be observed in Fig. 3.1. Finally, a solution to such optimisation problems requires a sensitivity analysis to determine the search directions. Sensitivities are defined as the derivatives of the objectives and constraints with respect to the design variable ρ . Due to assumptions in the SIMP model that presume the Poissons ratio is independent of the density, a condition on the range of acceptable values of p is formed [41, 44]. This range of values in 2D is given as

$$p \geq \max \left\{ \frac{2}{1 - v^0}, \frac{4}{1 + v^0} \right\} \quad (3.4)$$

where v^0 is the Poisson ratio of the given isotropic base material. Typically, $v^0 = 1/3$ and as such $p \geq 2$ for 2D cases.

3.1.2 Density Filtering

The issue with the SIMP scheme is the lack of solutions to a distributed problem [41, 44]. This makes the solutions to the optimisation problem mesh-dependent. The reason for this is the increasing number of holes without any change in structural volume, which increases the efficiency of the structure [41]. When a compliance-based optimisation problem is run on a computer, the solution with finer FE meshes will have a larger number of holes. This mesh refinement leads to the development of finer-scale structures [41, 45] as presented in Fig. 3.2.

To generate solutions that are independent of the mesh, the space of acceptable densities must be reduced. This is typically achieved through additional constraints on the optimisation problem. Methods

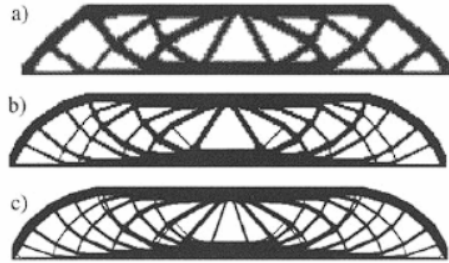


Figure 3.2: Solution to MBB beam with increasing mesh refinement [41]

such as perimeter control and gradient constraints apply explicit limits on the densities and can have noticeable effects on the final design [41]. A better approach is to limit the variation of densities, which is achieved through density filtering. Several filters have been investigated in past studies. For the study presented in this report, the Helmholtz filter is used due to its robustness and ease of implementation within the Firedrake environment. The implementation of this filtering technique is also noted to be computationally more efficient compared to other filters [40, 45, 46]. To do so, the density filter is defined implicitly as the solution to a Helmholtz-type PDE [45, 47] given as

$$-r^2 \nabla^2 \tilde{\rho} + \tilde{\rho} = \rho \quad (3.5)$$

with homogeneous natural boundary conditions

$$\frac{\partial \tilde{\rho}}{\partial \vec{n}} = 0$$

where $\tilde{\rho}$ represents the filtered density and ρ represents the unfiltered density. This PDE is solved in the design domain and it filters densities in a radius defined by r . The solution does not change the total volume present in the computational domain [45]. Fig. 3.3 shows the effect of a Helmholtz-type filter on a given density distribution. It shows that it increases the availability of intermediate densities (grey material) with an increasing filter radius.

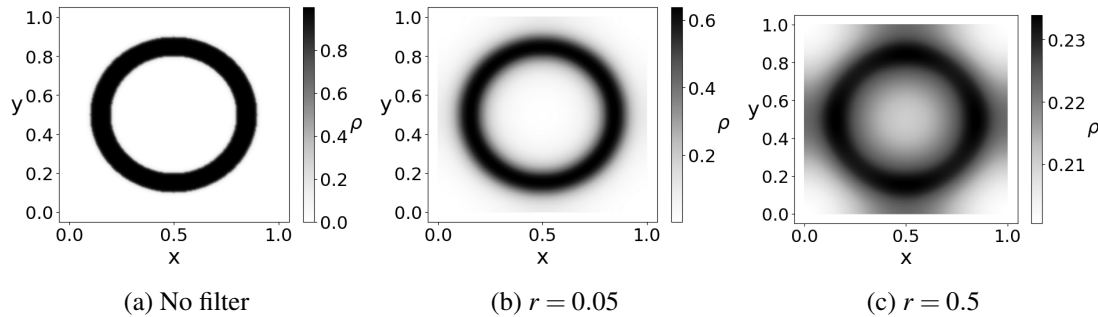


Figure 3.3: Effect of Helmholtz filter on density distribution

The filtering process generates intermediate densities that are significantly penalized according to Eq. 3.2 because they are uneconomical. This behaviour then reduces the variations seen in the densities, thereby reducing the mesh dependency of the results achieved through the optimisation problem. Another issue faced by topology optimisation problems utilising the finite element method is the formation of checkerboard patterns in the design space. This problem is typically due to bad numerical modelling and is not present when using fine meshes for finite element modelling of the forward problem [41, 48, 49]. Checkerboard effects on a cantilever beam are presented in Fig. 3.4.

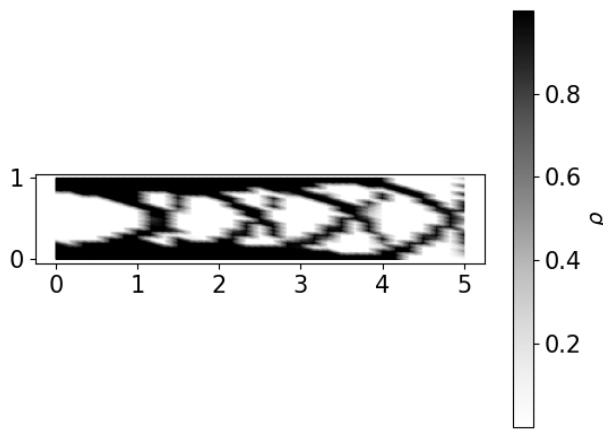


Figure 3.4: Checkerboard effect in a cantilever beam

3.1.3 Solving optimisation problems

Previous studies have solved this problem using methods such as the optimality criteria and the method of moving asymptotes [41]. IPOPT is chosen as the optimisation algorithm because it allows easy integration with the Firedrake environment and it behaves well for multi-constraint optimisation problems [50]. The sensitivities of the objectives and constraints required by IPOPT to determine search directions are provided by the Firedrake adjoints module. IPOPT has also been utilised to create successful topology optimisation programs in previously conducted studies [51]. Fig. 3.5 shows the process utilised by the Python code to solve a general topology optimisation problem.

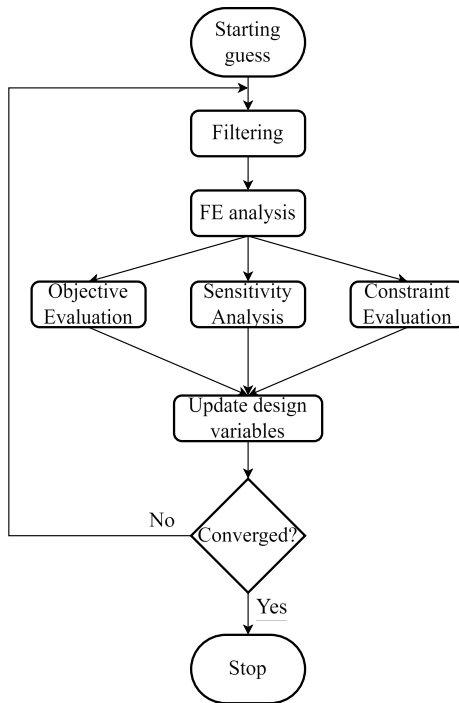


Figure 3.5: Flowchart describing the optimisation process

A brief introduction to IPOPT

This section provides a brief introduction to the mathematical optimization methods used in the IPOPT code. For a comprehensive explanation, refer to [50]. Consider an optimization problem formulated as follows:

$$\begin{aligned} \min_{x \in \mathbb{R}^n} & f(x) \\ \text{s.t. : } & c(x) = 0 \\ & x \geq 0 \end{aligned} \tag{3.6}$$

solutions will be found through a sequence of barrier problems in the form

$$\begin{aligned} \min_{x \in \mathbb{R}^n} & \phi_\mu(x) := f(x) - \mu \sum_{i=1}^n \ln(x^{(i)}) \\ \text{s.t. : } & c(x) = 0 \end{aligned} \tag{3.7}$$

with a decreasing sequence of barrier parameters μ which converge to zero. This is the same as applying a homotopy method to Eq. 3.6,

$$\begin{aligned} \nabla f(x) + \nabla c(x)\lambda - z &= 0 \\ c(x) &= 0 \\ XZe - \mu e &= 0 \end{aligned} \tag{3.8}$$

where λ and z represent Lagrange multipliers for the constraints represented in Eq. 3.6. The term $\nabla f(x)$ represents the jacobian of the function being minimised and $\nabla c(x)$ is the jacobian of the constraints of the optimisation problem in Eq. 3.6. Finally, to solve this problem, IPOPT utilises Newton's methods applied to the set of Eqs. 3.8. At each iteration, k , let (x_k, λ_k, z_k) denote the current solution estimate, and $(d_k^x, d_k^\lambda, d_k^z)$ denote the search directions of the algorithm. The solution can then be obtained by solving the following set of linear equations:

$$\begin{bmatrix} W_k & A_k & -I \\ A_k^T & 0 & 0 \\ Z_k & 0 & X_k \end{bmatrix} \begin{Bmatrix} d_k^x \\ d_k^\lambda \\ d_k^z \end{Bmatrix} = - \begin{Bmatrix} \nabla f(x_k) + A_k \lambda_k - z_k \\ c(x_k) \\ X_k Z_k e - \mu_k e \end{Bmatrix} \tag{3.9}$$

where

$$A_k = \nabla c(x_k) \quad W_k = \nabla^2(f(x) + c(x)\lambda - z)$$

3.1.4 Comparison of Solutions

When the optimisation process described in section 3.1.3 is completed the solution for the test case is obtained as shown in Fig. 3.6a. It is compared to the solution to the same problem available in the literature, shown in Fig. 3.6b. The figures show that the base topology optimisation code produces similar results. The base topology optimisation code can then be augmented to perform topology optimisation for stress constraints in the screw body. This is achieved through the introduction of a new objective function and several new constraints. However, the material interpolation scheme given in Eq. 3.2 remains unchanged.

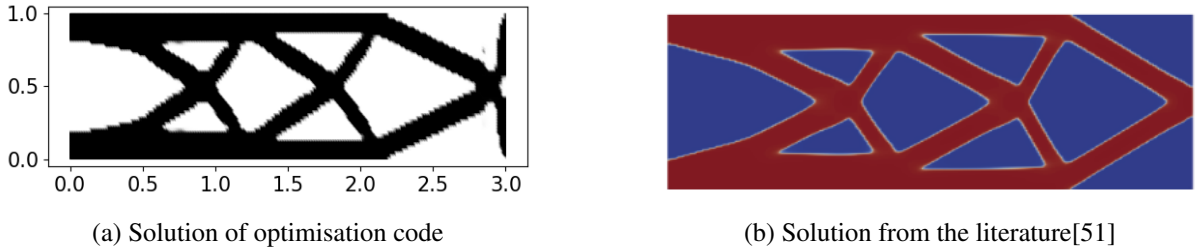


Figure 3.6: Comparison of solutions

3.2 Finite Elements for Linear Elasticity

To model the displacements and stresses within the design space of the screw, numerical modelling of the equilibrium equations must be used. The method used is the well-established finite element method. The finite element problems were solved using the Python finite element solver `Firedrake` [52]. This section aims to familiarise the reader with the governing equations of linear elasticity as well the final Galerkin weak form of the equations that are solved in `Firedrake`. The models predict material behaviour in the linear-elastic regime and as such, make these 4 assumptions [53].

1. Any deformation will be small.
2. The material is within its linear regime of behaviour.
3. Dynamic effects are negligible.
4. No overlaps or folding occurs during the deformation of the solid.

The partial differential equation for static linear elasticity is defined below

$$\begin{aligned} -\nabla \cdot \sigma &= f \quad \text{in } \Omega \\ \sigma &= 2\mu\varepsilon + \lambda I \nabla \cdot \mathbf{u} \quad \text{in } \Omega \\ \mathbf{u} &= \mathbf{g} \quad \text{on } \partial\Omega_D \\ \sigma \cdot \mathbf{n} &= \mathbf{t} \quad \text{on } \partial\Omega_N \end{aligned} \tag{3.10}$$

where \mathbf{g} describes the prescribed displacements on the Dirichlet boundary, $\partial\Omega_D$. The traction forces are represented by \mathbf{t} on the Neumann boundary, $\partial\Omega_N$. To form the Galerkin weak form, introduce the function v such that $v = 0$ on $\partial\Omega_D$, and integrate over the domain Ω .

$$\int_{\Omega} (-\nabla \cdot \sigma) \cdot v \, d\Omega = \int_{\Omega} f \cdot v \, d\Omega \tag{3.11}$$

The stress tensor for 2D linear elasticity is defined as

$$\sigma = \begin{bmatrix} \sigma_{xx} & \sigma_{xy} \\ \sigma_{xy} & \sigma_{yy} \end{bmatrix}$$

By invoking Gauss's theorem and using the stress tensor, the PDE can be finally represented in the following form

$$\underbrace{\int_{\Omega} \sigma(\mathbf{u}) : \varepsilon(\mathbf{v}) \, d\Omega}_{a_E(u, v)} = \underbrace{\int_{\Omega} f \cdot v \, d\Omega + \int_{\partial\Omega_N} t \cdot v \, dS}_{l(v)} \tag{3.12}$$

where the term $\int_{\Omega} f \cdot v \, d\Omega$ represents body forces acting on the entire domain and the term $\int_{\partial\Omega_N} t \cdot v \, dS$ represents traction forces acting on the Neumann boundary, $\partial\Omega_N$. The stress tensor, σ , is represented using Lamé parameters given by

$$\lambda = \frac{Ev}{(1+v)(1-2v)} \quad \mu = \frac{E}{2(1+v)} \quad (3.13)$$

The weak form of the 2D linear elasticity shown in Eq. 3.12 can then be easily modelled within the Firedrake environment. This equation was used for calculating the displacements for both the test code and the final screw design code. The type of elements and the order of polynomial functions used for modelling will be discussed in section 3.3.1, along with the mesh refinement procedure to ensure accurate modelling of the displacements in the domain.

3.3 Topology optimisation of bone screws

3.3.1 Problem setup

Chapters 1 and 2 introduced the problem associated with bone screws and the main focus of this report. It also introduced previous experimental studies and the reason behind screw failure during pullout. To rephrase the problem, failure during pullout occurs due to the shear stresses in the bone between the threads. Photoelastic models of screw pullout confirm that the shear stresses are concentrated over the first threads and the area between the thread crests is subject to extremely high shear stresses[31]. This behaviour is confirmed through finite element simulations[54] and further simulations of a simplified, unoptimised screw body undergoing pullout are presented in chapter 4 for further discussion and comparison to optimised screw bodies. The goal of applying topology optimisation is to create a structure within the screw body to minimise these stress concentrations near the head of the screw.

The first step in this process is to create a finite element mesh that models the behaviour of an implanted screw during pullout. It was seen earlier that parameters such as threads, screw diameters and screw pitch would impact the pullout resistance of a screw. Since the body of the screw is of interest the model does not contain any screw parameters that may influence the overall result. This simplifies the mesh drastically. Simple screw meshes have also been used in finite element simulations before and they have yielded comparable results to more complex models [55].

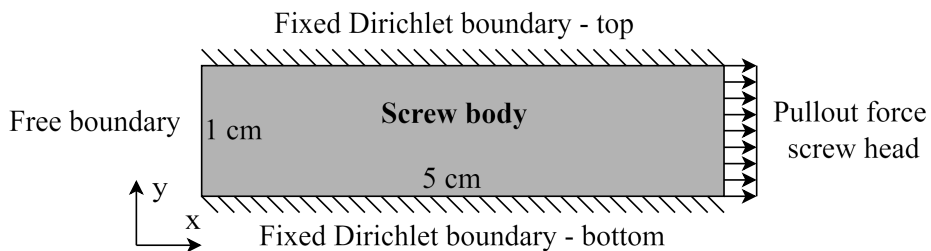


Figure 3.7: finite element model for bone screw optimisation

Fig. 3.7 shows the layout of the boundary conditions and loads on the finite element mesh. The top and bottom boundaries are modelled as fully fixed Dirichlet boundary conditions. There is a load applied to the right-hand side boundary, making it a Neumann boundary. There is no boundary condition on the left-hand side boundary and it is simply modelled as a free boundary. The final mesh is 5cm × 1cm and its resolution was finalised through a mesh convergence study of the displacement at the Neumann

boundary. For simplicity, the number of elements in the x-direction was chosen to be 3 times the number of elements in the y-direction. The results of the convergence study shown in Fig. 3.8 were then obtained by varying the number of elements in the y-direction. The mesh convergence study also presents the location of the chosen mesh resolution on the curve. The number of elements in each direction and the dimensions of the final mesh are summarised in Tab. 3.1. The convergence study and all subsequent simulations have used triangular elements. Polynomial equations used for the approximations were first-order and continuous. It was decided that the screw would be modelled using a titanium alloy discussed in chapter 2. Titanium alloys were chosen due to their proven effectiveness and popularity in the industry, as discussed in chapter 2. The physical properties of the chosen alloy are presented in Tab. 3.2.

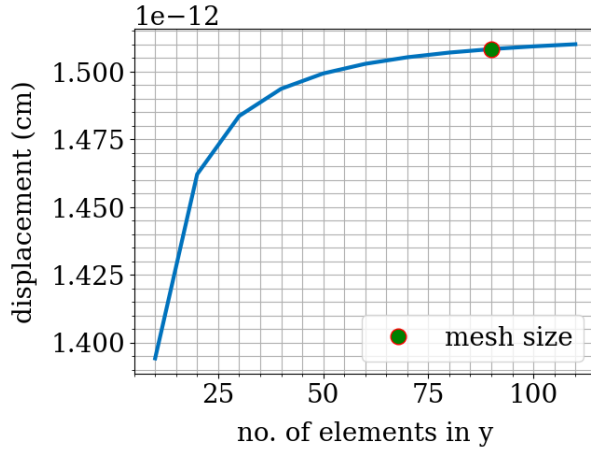


Figure 3.8: Mesh convergence study

Table 3.1: Mesh properties

Dimension	Size (cm)	Elements
Length	5.0	180
Width	1.0	90

Table 3.2: Titanium alloy properties

Young's Modulus (GPa)	Poisson Ratio
113	0.3

3.3.2 Objective function, J

The next step was to create a new optimisation problem to remove the large stress concentrations observed around the threads. Previous studies [39] into stress-based optimisation have investigated the use of objective functions of the form

$$J = (C(\varepsilon_i) - C^*(\varepsilon_i))^2 \quad (3.14)$$

where $C(\varepsilon_i)$ represents the current stress state of the structure and $C^*(\varepsilon_i)$ represents a target stress state. When Eq. 3.14 is set as an objective function for a topology optimisation problem, it optimises the structure towards the target stress state. Using this methodology, a new objective function to target an averaged shear stress state along the fixed boundaries was formulated. This new objective function is

$$J = \int_{\partial\Omega_D} (\sigma_{xy} - \bar{\sigma}_{xy})^2 \, dS \quad (3.15)$$

$$\bar{\sigma}_{xy} = \frac{\int_{\partial\Omega_D} \sigma_{xy} \, dS}{\int_{\partial\Omega_D} dS} \quad (3.16)$$

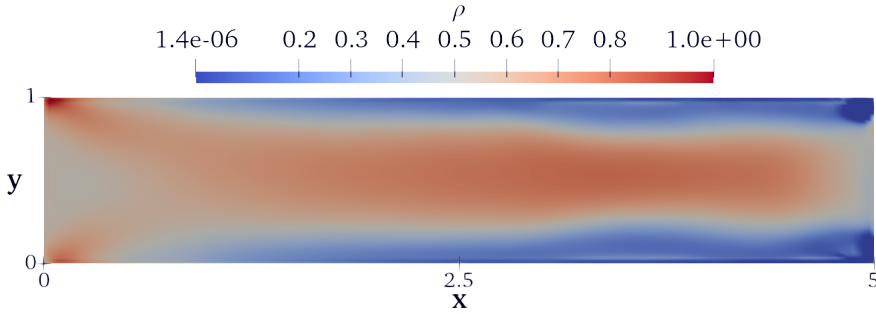


Figure 3.9: Fully grey design

where σ_{xy} is the shear force and $\bar{\sigma}_{xy}$ is the averaged shear force. Note how this integral is only defined over the Dirichlet boundary and will only apply to the top and bottom boundaries of the domain shown in Fig. 3.7—however, this type of stress-based objective function does not naturally penalise intermediate densities, unlike the minimum compliance problem[56]. Fig. 3.9 shows the effect of applying this objective function directly in the solver, without any regularization methods to promote discrete designs. It is clear from the plot that no discernible structures are forming in the design domain. The intermediate density problem is well-documented in the literature and many solutions have been developed to promote the growth of discrete (0-1) designs[38, 39, 56, 57]. The following subsections will describe the methods employed in the literature and how they are utilised in the context of bone screw optimisation to pursue discrete designs.

3.3.3 Threshold Projection

In standard compliance problems, it can be easy to perform simple post-processing steps to remove any lingering intermediate densities and to obtain a smooth design. However, in more complicated simulations performing post-processing might produce incorrect structures [58]. The grey material produced from the usage of a Helmholtz-type filter to remove mesh dependency is no longer naturally penalised through the objective function. Studies have been carried out to investigate the use of morphological functions to create discrete designs. These functions are namely dilation and erosion [58]. A dilation function typically grows the density distribution around solid elements, while erosion typically removes density around void elements. These functions typically need to be defined such that their derivatives exist to evaluate sensitivities.

One such function that has been formulated for use in SIMP-based topology optimisation is the projection filter defined as

$$\bar{\rho} = \frac{\tanh(\beta\eta) + \tanh(\beta(\tilde{\rho} - \eta))}{\tanh(\beta\eta) + \tanh(\beta(1 - \eta))} \quad (3.17)$$

where $\tilde{\rho}$ represents the filtered densities from the Helmholtz filter and $\bar{\rho}$ represents the projected densities[38, 56]. The parameter η is a threshold determining the range of densities projected between 0 and 1. When $\tilde{\rho} > \eta$ densities will be projected to 1 and when $\tilde{\rho} < \eta$ densities will be projected towards 0. The parameter β controls the linearity of the projection and as $\beta \rightarrow \infty$, the projection filter encourages discrete designs. The effect of β on the threshold projection is presented in Fig. 3.10. It is clear that increases in β result in an aggressive projection of intermediate densities to either 0 or 1. This function is very similar to the logistic sigmoid functions utilised in AI models for the mapping of binary choices in neural networks.

This method has been utilised successfully to create discrete optimised microstructures before [38, 39, 58]. For visualisation purposes, the projection filter has been applied to a material distribution passed

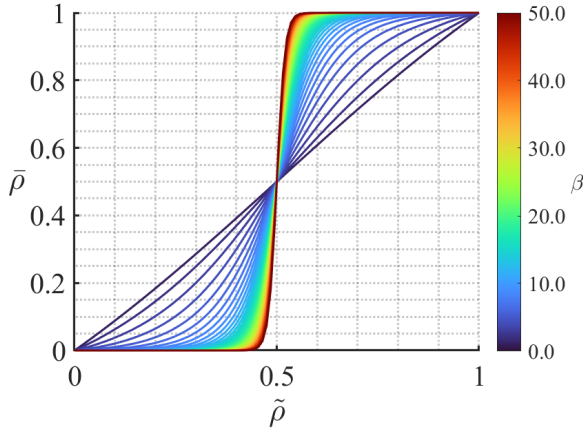


Figure 3.10: Effect of beta on the linearity of the projection

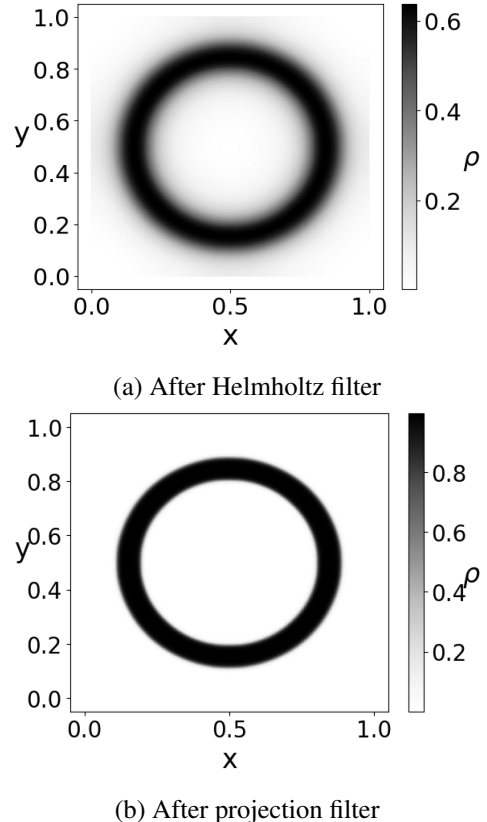


Figure 3.11: Effect of projection filter on grey material ($\beta = 20, \eta = 0.5$)

through a Helmholtz filter and the outcome is shown in Fig. 3.11b. The effect of the projection filter is clear as the final output is fully discrete and any intermediate densities present in Fig. 3.11a have been projected to either 0 or 1. In practice, large β values cannot be implemented directly due to the aggressive projection shown in Fig. 3.10. Typically, programs using this filter work through multiple rounds of optimisation, each with an increasing value of β [39, 58].

3.3.4 Intermediate Density Penalisation

The bone screw design showed high levels of intermediate densities, even though the use of a projection filter in the optimisation process should encourage the growth of a discrete design. This leads to an added constraint in the process to further penalise intermediate densities. This constraint is given as

$$\phi = \int_{\Omega} [4\bar{\rho}(1-\bar{\rho})]^{1-\alpha} d\Omega \leq \phi_{max} \quad (3.18)$$

where $\bar{\rho}$ is the filtered density output from the projection filter in Eq. 3.17. This constraint is a measure of the intermediate density present in the design space Ω . When $\bar{\rho} \rightarrow 0$ or 1 the design is purely discrete and the integrand in Eq. 3.18 tends to zero, indicating no intermediate densities present in the domain. When $\bar{\rho} = 0.5$ the integral will give a measure of these intermediate densities across the domain. The parameter α is used for controlling the penalty of intermediate densities close to $\bar{\rho} = 0$ or 1. This control over the penalisation is highlighted in Fig. 3.12.

By adding a constraint on the value of ϕ , the amount of intermediate densities can be limited in the design space. This process has been utilised successfully in the creation of optimised microstructures [38] and in promoting binary designs in general optimisation studies [59]. The constraint is implemented

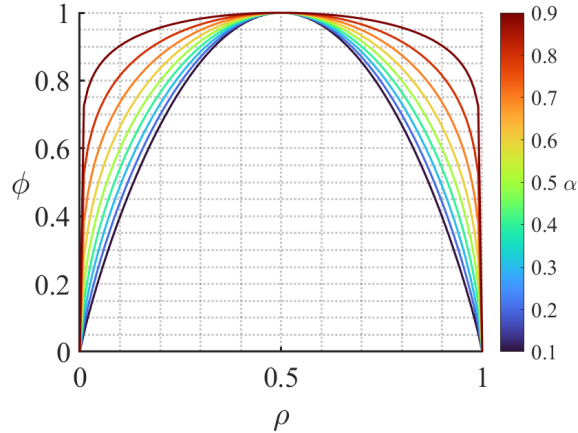


Figure 3.12: Intermediate density penalisation with varying α

similarly to the threshold projection, where the maximum value of ϕ is set to be very large at the start of the optimisation process and is decreased using consecutive rounds of optimisation. Since ϕ is a measure of intermediate densities, decreasing the maximum allowed value of ϕ limits the amount of grey material in the design.

With methods now in place to promote discrete designs, the following sections will explore the additional constraints introduced to the system. Some of the constraints aim at augmenting the design to increase its performance in pullout, while others are essential to guide the optimisation process towards a sensible outcome.

3.3.5 Auxeticity constraint

Solid materials with positive Poisson ratios typically exhibit the behaviour of contracting in the direction orthogonal to the applied tensile load. This behaviour is a disadvantage in the context of designing bone screws to resist pullout. The objective function shown in Eq. 3.15 functions well, creating a screw that distributes shear stresses through the boundary and would prevent the failure of the bone-screw interface. However, decreases in bone screw diameter would result in the implant being pulled out of the implantation site. Thus, the need for an expanding screw body is clear. Screws with such qualities have shown success in past studies and their designs were elaborated on in chapter 2.

To create an expanding screw structure, an extra set of constraints must be added to the final optimisation problem. These constraints are formulated to force the structure created to exert opposing vertical forces on the top and bottom boundaries of the domain shown in Fig. 3.7. This set of constraints is written as

$$\text{LB} \leq \int_{\partial\Omega_{D_{upper}}} [\sigma_{xx} \quad \sigma_{yy}]^T \cdot \mathbf{n} \, dS \leq \text{UB} \quad (3.19)$$

$$\text{LB} \leq \int_{\partial\Omega_{D_{lower}}} [\sigma_{xx} \quad \sigma_{yy}]^T \cdot \mathbf{n} \, dS \leq \text{UB} \quad (3.20)$$

$$-1 \leq \int_{\partial\Omega_{D_{upper}}} [\sigma_{xx} \quad \sigma_{yy}]^T \cdot \mathbf{n} \, dS + \int_{\partial\Omega_{D_{lower}}} [\sigma_{xx} \quad \sigma_{yy}]^T \cdot \mathbf{n} \, dS \leq 1 \quad (3.21)$$

where the integration of the stresses over a boundary evaluates the forces acting on that boundary, multiplying the stress vector by the normal vector, \mathbf{n} , ensures that the forces calculated are normal to the boundary. The constraint represented in Eqs. 3.19 and 3.20 evaluate the vertical forces at the upper boundary and lower boundaries respectively. The constraint limits the force to a value between a given

upper and lower bound. Setting strict constraints is a possibility, however, it is not possible to know the exact optimum force the structure can produce for a given stimulus. Therefore, the constraint is limited to a range of values. In practice, it was found that the optimisation routine preferred to limit the structure towards the given lower bound. Chapter 4 will explore structures created by increasing the lower bound of these constraints.

Since the exact force magnitude is not defined before the start of the simulation, a new constraint is added to ensure that the vertical forces applied on the boundaries are opposing and equal in magnitude. This final equilibrium constraint is presented in Eq. 3.21. The equilibrium condition was first set to be equal to zero, however, it was found that the optimiser struggled to create a structure given a hard constraint. It was instead decided to relax the equilibrium constraint by limiting it to a small range of values around zero.

3.3.6 Displacement Constraint

Initially, the simulation was run without any constraints on the displacements allowed at the Neumann boundary. This leads to a single core structure growing in the design space, as shown in Fig. 3.13. This central core of material experiences significant displacement due to the weaker surrounding material. Despite this weakness, the surrounding material still exerts a force because the central core's displacement is very large. This force remains nearly constant because the shear stress is consistent along the length of the core and its walls due to the substantial displacement. This structure is an effect of modelling the simulation using a linear elastic model.

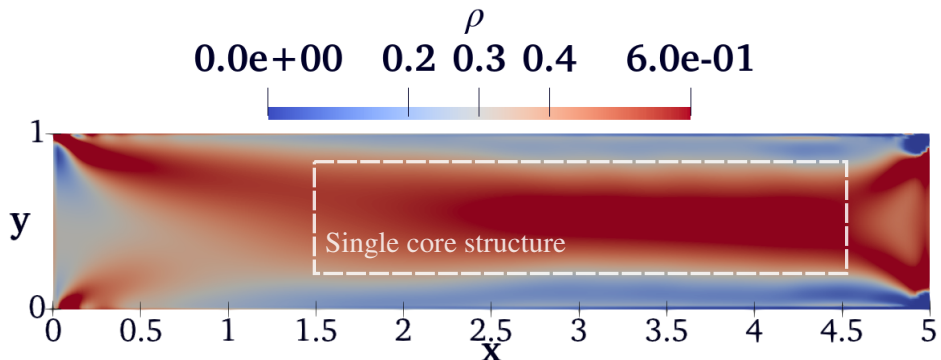


Figure 3.13: Formation of a single core structure in the design space

To model a more accurate representation of the problem, the large displacements seen at the Neumann boundary have to be limited. This is achieved through an extra constraint in the final optimisation problem. The maximum displacement value for the constraint was identified through a finite element simulation of a solid block of material under the same loading conditions as the ones in Fig. 3.7. In practice, it was found that slight loosening of this constraint was required and it was achieved by multiplying the displacement constraint with a factor K . This factor would allow the body of the screw to grow across the entire domain. The final constraint on the displacements on the force boundary is

$$0 \leq \int_{\partial\Omega_N} \mathbf{u} \cdot \mathbf{n} \, dS \leq Ku_x \quad (3.22)$$

where u_x is the displacement of a solid block of material with the same properties as shown in Tab. 3.2 undergoing a pullout test. The final value of K and u_x are presented in Tab. 3.4.

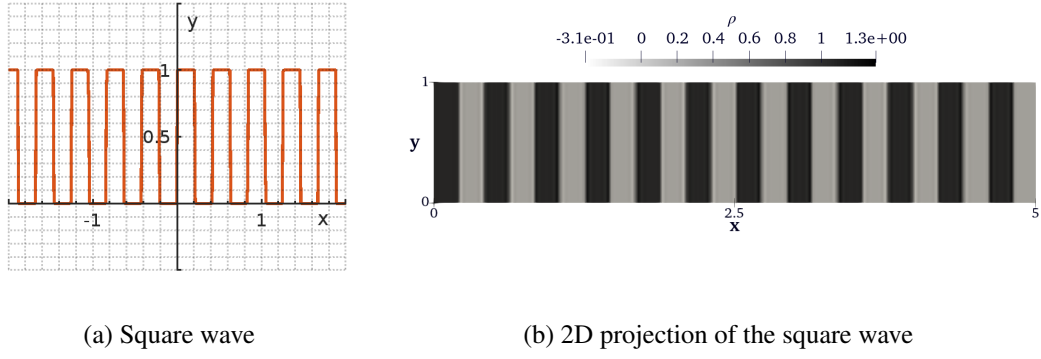


Figure 3.14: Square wave ($a = 15$) and its 2D projection onto the design domain Ω

3.3.7 Material deposition constraint

During the optimisation process, it was noticed that the optimiser struggled to grow the screw body within the design domain. To promote the growth of structures across the domain a constraint was created that forces the growth of densities across the top and bottom boundaries. The pattern of material deposition was controlled through a hyperbolic function. It is given as

$$y = \frac{\tanh(1000 \sin^{-1}(\sin(ax))) + 1}{2} \quad (3.23)$$

The sine function creates a periodic wave with a frequency a that oscillates in the range $[-1, 1]$. When its inverse is calculated, the periodic wave is mapped onto a set of angles that oscillate within the range $[-\pi/2, \pi/2]$. The hyperbolic tangent is used for scaling and compressing the output from the inverse sine function. The factor of 1000 is used for faster saturation, which maps the oscillations in the range $[-1, 1]$. Finally, a set of transformations is added to the function to create oscillations in the range $[0, 1]$, which correspond to the values of a discrete distribution of densities in the design space. Eq. 3.23 is plotted in Fig. 3.14a, where a square wave of frequency $a = 15$ can be observed. The function in Eq. 3.23 can then be projected onto the design domain Ω . The projection of this forcing function results in bands of density as shown in Fig. 3.14b forming on the design space. Locations where $\rho_{projected} = 1$ in the design space, as shown in Fig. 3.14b, correspond to locations where $y = 1$ in the hyperbolic function depicted in Fig. 3.14a.

Finally, to force material deposition at these points along the top and bottom boundaries, a new constraint is introduced in the form

$$-1 \leq \int_{\partial\Omega_D} (\bar{\rho} - \rho_{projected})^2 \, dS \leq 1 \quad (3.24)$$

where $\bar{\rho}$ is the filtered density and $\rho_{projected}$ is the projected density. The integral is formulated to be evaluated at the Dirichlet boundaries. When the optimiser deposits material at locations along the boundary where $\rho_{projected} = 1$, the integrand in Eq. 3.24 will tend to zero, thus meeting the constraint bounds. Therefore, the material will be deposited along the Dirichlet boundaries in bands matching the projection in Fig. 3.14b. The deposited material acts as contact points and promotes the growth of the structure through the design space.

3.3.8 Final optimisation problem

The new objective functions, filters and constraints were added to the baseline topology optimisation code discussed in section 3.1.3. To control the amount of intermediate densities, parameters from the projection filter and intermediate density penalisation constraint have to be changed through continuous k sub-iteration steps, with each sub-iteration containing i_{max} iterations in the optimiser, IPOPT. To do so, a starting set of values for the parameters is chosen. They are presented in Tab 3.3.

Table 3.3: Optimisation parameters for promoting discrete designs

Simulation Parameter	Starting value	Continuation values
α	0.00001	$0.18k - 0.08$
ϕ_{max}	10	$\phi_{i_{max}}^k$
β	3	$2\beta^k$
i_{max}	120	40

The first sub-iteration is run for 120 optimiser iterations on IPOPT and any subsequent sub-iteration is only run for 40 IPOPT iterations. The constraint on the intermediate density penalization, ϕ_{max} , was initially set to be very large, as starting with a strict constraint was found to be overly restrictive. As the simulation progresses, the value of ϕ_i decreases due to decreasing intermediate densities. The final recorded value from each sub-iteration, $\phi_{i_{max}}^k$, was then used as the constraint for any subsequent sub-iteration. The initialisation of the starting guess of density distributions for each sub-optimisation problem follows a similar method, where the preceding design is used to warm start any subsequent iteration. Other values such as β and α are simply increased linearly across the sub-iterations, as shown in Tab. 3.3. This method allows the topology optimisation code to effectively penalise intermediate densities while finding the most effective density distribution to solve the optimisation problem. Similar methods have been applied to obtain discrete designs before [38]. This process is presented in the flowchart in Fig. 3.15 for easier visualisation. For clarity, the final optimisation problem solved by the optimiser during each k^{th} sub-iteration is shown in Eq. 3.25. This equation presents the objective and the constraints as an optimisation problem. Individual equations have been named and linked to their relevant section in the report for reference.

The previous sections also introduced several constraints and filters that would be used within the final optimisation routine. These constraints and filters have parameters that are constant through all k sub-iterations described above. These constant parameters and their chosen constant values are presented in Tab. 3.4. The parameters are presented in the order they were discussed in the report.

Table 3.4: Constant simulation parameters for each sub-iteration

Used in	Simulation Parameter	value
Helmholtz filter	r	0.044 cm
Displacement constraint	K	15
Displacement constraint	u_x	1.5×10^{-8} cm
Projection filter	η	0.5
Volume constraint	V	$0.7 \times 5 \times 1$

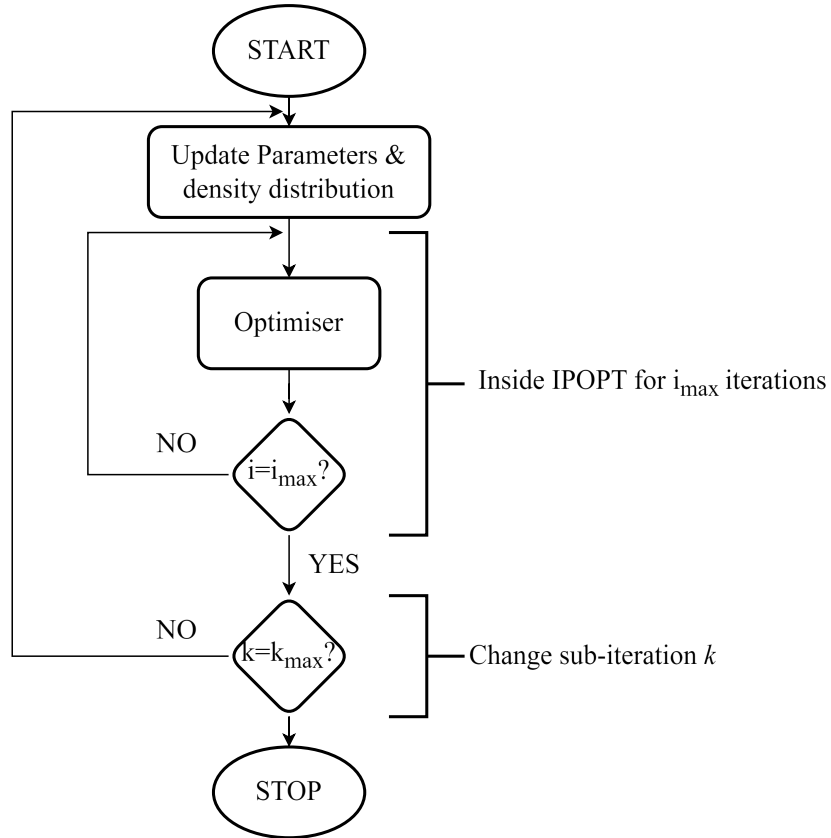


Figure 3.15: Flowchart of optimisation process

$$\begin{aligned}
 \min_{u \in U, \rho} \quad & J = \int_{\partial\Omega_D} \left(\sigma_{xy} - \frac{\int_{\partial\Omega_D} \sigma_{xy} dS}{\int_{\partial\Omega_D} dS} \right)^2 dS && \text{Shear stress objective function - 3.3.2} \\
 \text{s.t.} \quad & a_E(u, v) = l(v), \quad \forall v \in U_0 && \text{Equilibrium (FE) - 3.2} \\
 & E = E_{\min} + (E_{\max} - E_{\min})\rho^p && \text{SIMP Interpolation - 3.1} \\
 & \int_{\Omega} \bar{\rho} d\Omega \leq V && \text{Volume constraint - 3.1} \\
 & \phi = \int_{\Omega} [4\bar{\rho}(1-\bar{\rho})]^{1-\alpha} dS \leq \phi_{\max} && \text{Intermediate density penalty - 3.3.4} \\
 & \int_{\partial\Omega_N} \mathbf{u} \cdot \mathbf{n} dS \leq Ku_x && \text{Displacement constraint - 3.3.6} \\
 & -1 \leq \int_{\partial\Omega_D} (\bar{\rho} - \rho_{projected})^2 dS \leq 1 && \text{Material deposition constraint - 3.3.7} \\
 & LB \leq F_{upper} = \int_{\partial\Omega_{D_{upper}}} [\sigma_{xx} \ \sigma_{yy}]^T \cdot \mathbf{n} dS \leq UB && \text{Force on upper boundary - 3.3.5} \\
 & LB \leq F_{lower} = \int_{\partial\Omega_{D_{lower}}} [\sigma_{xx} \ \sigma_{yy}]^T \cdot \mathbf{n} dS \leq UB && \text{Force on lower boundary - 3.3.5} \\
 & -1 \leq F_{upper} + F_{lower} \leq 1 && \text{Vertical equilibrium - 3.3.5}
 \end{aligned} \tag{3.25}$$

Chapter 4

Results and Discussion

The goal of this chapter is to present the final designs created by the bone screw optimisation problem introduced in Chapter 3. The chapter aims to conduct a parametric study of the screw design so that the reader may observe how the screw design changes with given stimuli and constraints. It aims to comment on the discreteness of the constructed designs and methods of post-processing. The chapter will also investigate the optimised stress distributions along the Dirichlet boundaries, so that the reader may evaluate the effectiveness of the proposed screw geometries.

4.1 Problems with asymmetry

When the optimisation problem given in section 3.3.8 is solved on the domain shown in Fig. 3.7, it results in asymmetric designs. The design must be symmetric due to the symmetric boundary conditions of the problem. This asymmetric design was traced to a few causes—the first being asymmetric shear forces along the top and bottom of the domain. The objective function stated in Eq. 3.15 actively spreads stresses across the boundaries, however, it does not ensure symmetrically imposed shear forces along these boundaries. A new constraint was introduced to the problem to address this behaviour and ensure that these forces were equal in magnitude. Since the top shear force was always negative, the constraint was set as

$$\int_{\partial\Omega_{D_{lower}}} \sigma_{xy} dS + \int_{\partial\Omega_{D_{upper}}} \sigma_{xy} dS = 0 \quad (4.1)$$

This new constraint seemed to improve the design to a certain extent. However, despite imposing both vertical and shear force equilibrium constraints in the optimisation problem, the design remained asymmetrical. This asymmetric design is presented in Fig. 4.1 along with the line of symmetry of the domain.

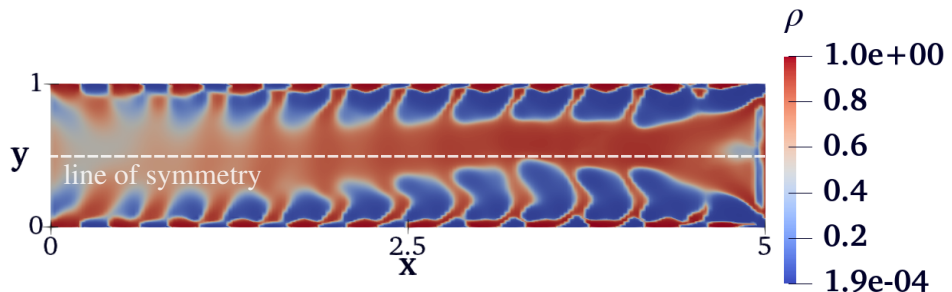


Figure 4.1: Asymmetric material distribution with annotated line of symmetry

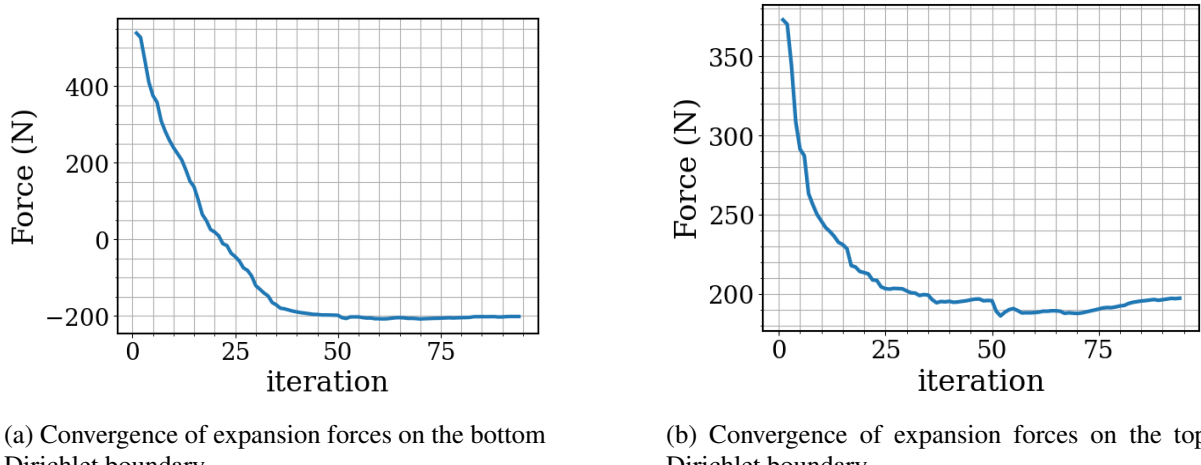


Figure 4.2: Expansion force histories

The issue could be due to the use of relaxed bounds for many of the constraints used in the optimisation problem, as shown in Eq. 3.25. Relaxed bounds were necessary, as the optimiser IPOPT would otherwise struggle to find solutions to the optimisation problem. The evolution of the expansion forces at the upper and lower boundaries was recorded during the simulation and findings are presented in Fig. 4.2. These plots present an instance of a non-equilibrium in the forces created in the design domain. It is clear that the expansion forces on the lower boundary achieve good convergence, however, the expansion forces on the upper boundary struggle to do so. By the end of the simulation, the expansion force on the upper boundary has yet to converge to 200 N. Therefore, the structure shown in Fig. 4.1 does not fully obey the vertical equilibrium constraint.

Instead of relying on the optimiser to impose constraints assuring symmetries, the model was halved. The symmetric loading and boundary conditions provide an excellent opportunity to utilise a simpler domain. This new model imposes a symmetry boundary condition through the centre of the original domain shown in Fig. 3.7 and is simply expressed as

$$u_y = 0 \text{ on } y=0.5 \text{ cm} \quad (4.2)$$

This new constraint permits the removal of certain equilibrium conditions, such as the equilibrium condition for the expansion and shear forces. The halved domain is also computationally efficient and convergence of the overall problem was improved greatly. The designs in the following sections of this chapter will present the material distribution across the full domain. This was achieved, for presentation purposes, by reflecting the design along the $y = 0.5$ cm line using the software Paraview. The stress concentrations for the parametric studies are evaluated for the bottom boundary, as all simulations were conducted on the bottom half of the domain shown in Fig. 3.7.

4.2 Unoptimised stress distributions in a bone screw

The subsequent sections will analyse the change in the stress distributions along an optimised screw structure. Therefore, it is important to identify the key characteristics of the stress field of an unoptimised bone screw during pullout. The unoptimised bone screw, for comparison purposes, is idealised as a solid block of material. Fig. 4.3a shows the shear stress distribution for the idealised, unoptimised screw body. The shear stress, σ_{xy} , has very high concentrations near the head of the screw, as shown by the extracted shear stress along the top and bottom boundaries of the idealised screw. The location of the shear stress concentrations validates the findings of the photoelastic models created to identify the stresses

around screws[31]. These stress concentrations are attributed towards the progressive degradation of surrounding bone.

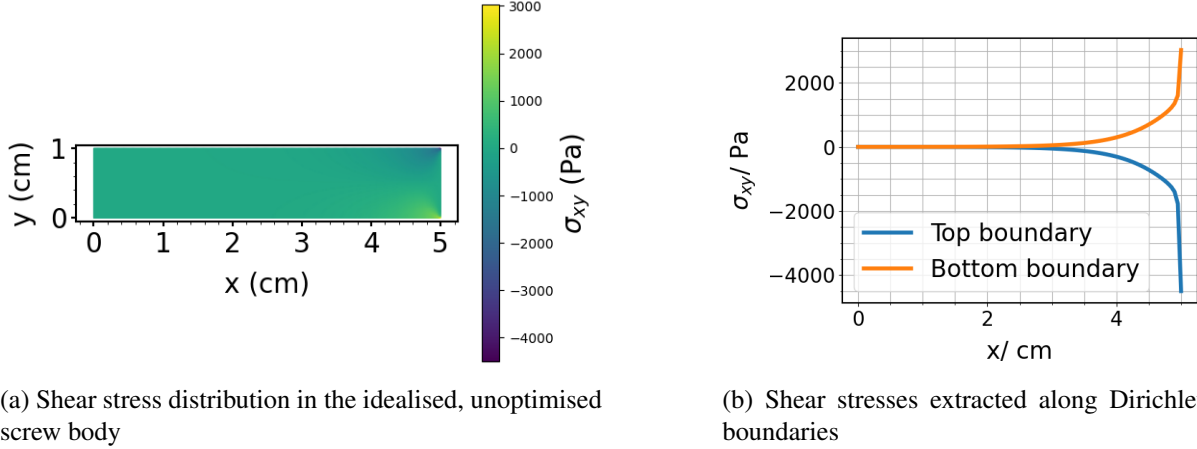


Figure 4.3: Evaluation of the shear stresses in an unoptimised screw body

4.3 Varying pullout force, P

The goal of this study is to create multiple designs of the screw body to different stimuli. Load, P , at the Neumann boundary is varied and the resulting screw topologies are presented. For simplicity and comparison of the designs, the expansion force F and frequency a are kept constant. Their respective values can be found in Tab. 4.1. The designs are analysed for $P = 1000, 1500, 2000, 2500$ and 3000 N and the results of this analysis are presented in Figs. 4.4 - 4.8. The range of values chosen for this design study is representative of the range of maximum pullout forces observed in studies that conducted experimental pullout testing of bone screws[4, 29].

Table 4.1: Constant simulation parameters

\mathbf{F} (N)	\mathbf{a}
200	15

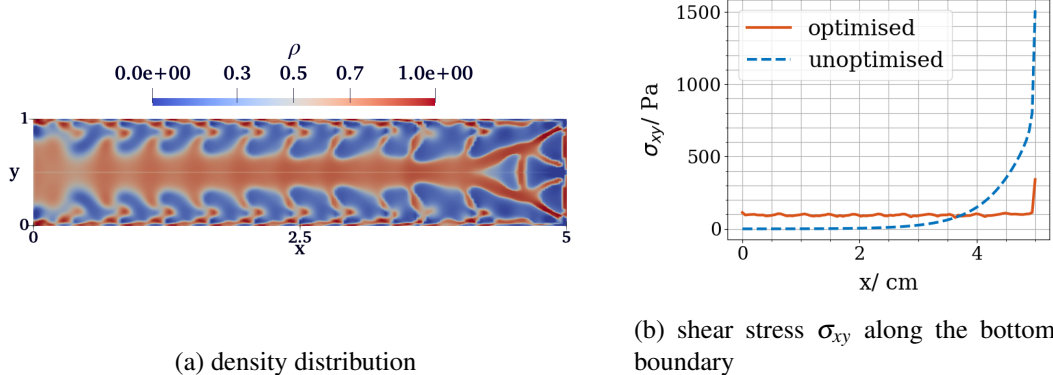
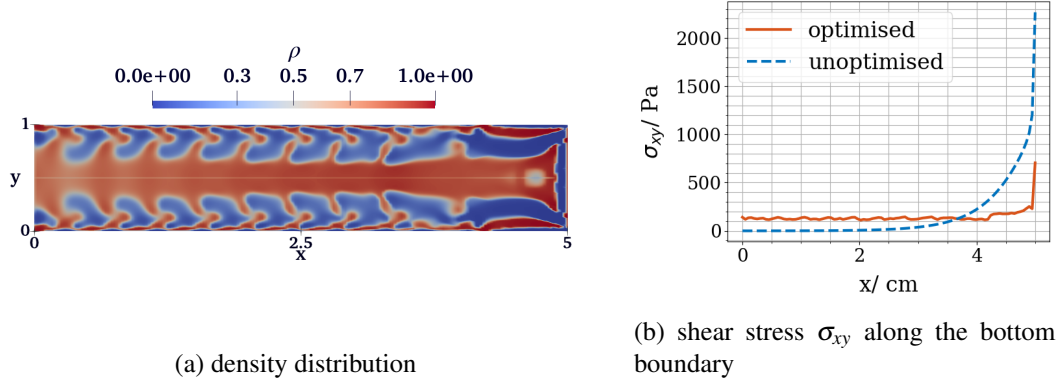
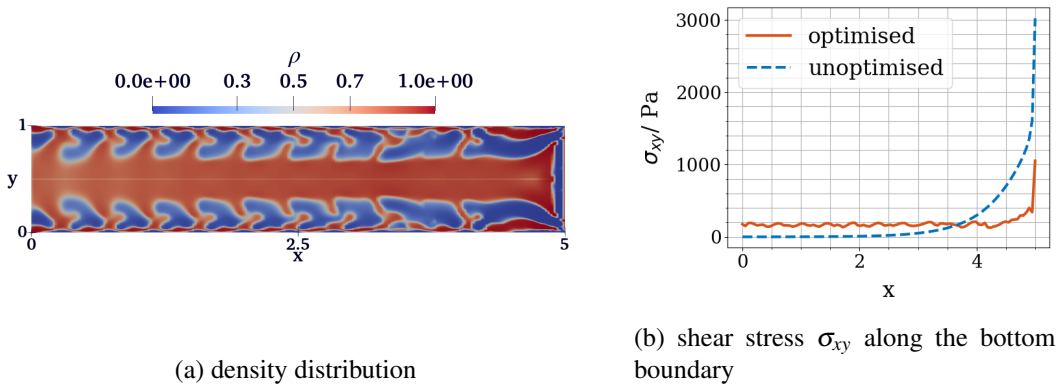
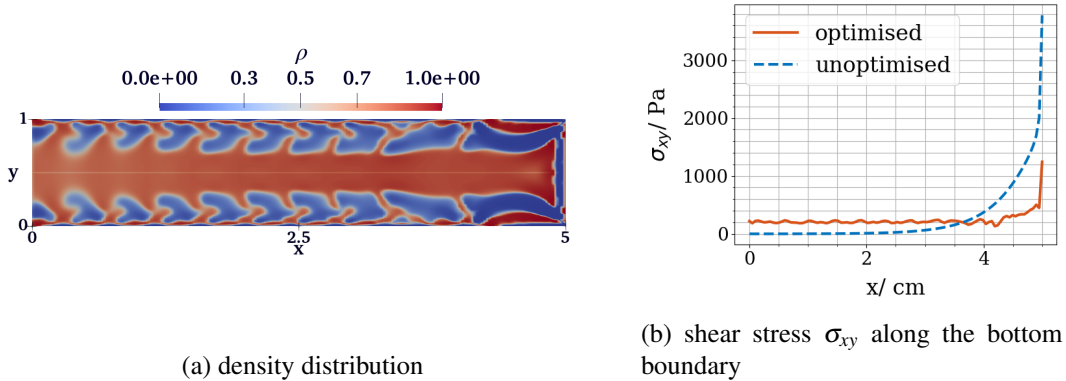
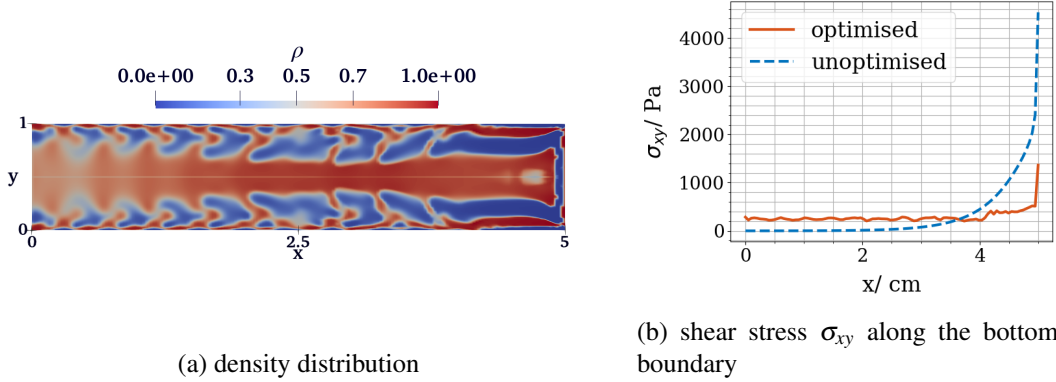


Figure 4.4: Design and stress distribution for $P = 1000$ N

Figure 4.5: Design and stress distribution for $P = 1500\text{N}$ Figure 4.6: Design and stress distribution for $P = 2000\text{N}$ Figure 4.7: Design and stress distribution for $P = 2500\text{N}$

Figure 4.8: Design and stress distribution for $P = 3000\text{N}$

The results for each pullout force magnitude present the corresponding material distribution alongside the shear distributions on the bottom Dirichlet boundary. The stress distributions presented in Figs. 4.4b to 4.8b indicate that the optimized structures exhibit low yet consistent shear stresses originating from the free boundary on the left-hand side of the domain. This contrasts with the unoptimized design, which exhibits no shear stresses at the free edge. This shows that the optimized structure has successfully spread shear stresses across the bottom boundary. Moving towards the Neumann boundary, the plots show an increase in shear stress around the 4 cm point. This is then followed by a final, abrupt increase in the shear stress. This final optimized shear stress peak is much lower than the unoptimized peaks for each case.

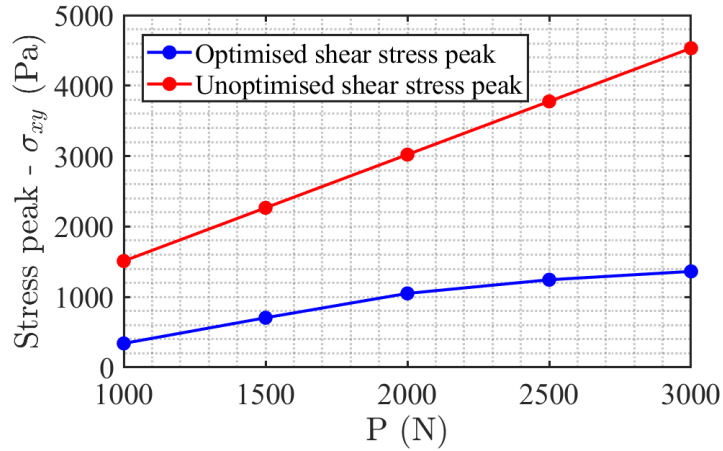


Figure 4.9: The difference in shear stress peaks between the optimised and unoptimised screws

Fig. 4.9 presents the peak shear stress values for each magnitude of P for both the optimised and unoptimised structures. It shows that each optimised shear stress peak is much lower than its unoptimised counterpart. The plot also highlights an increasing difference between the optimised and unoptimised stress peaks with increasing pullout force. The structures created for carrying higher loads seem to be more efficient compared to the structures optimised for lower loads. In summary, this analysis highlights the ability of the novel material distributions to spread shear stresses and reduce the magnitude of the stress peaks along the boundaries of a screw.

4.4 Varying expansion forces, F

The goal of this study is to create multiple screw designs for varying expansion forces while holding $P = 2000$ N and $a = 15$ constant, allowing for a meaningful comparison between cases. To vary the expansion force, the lower bound of the constraint in Eq. 3.20 is changed. The resulting density distributions and their shear stress distributions are presented in Figs. 4.10 - 4.12. The final design shown in Fig. 4.12 shows the optimisation results for a case where $P = 3000$ N.

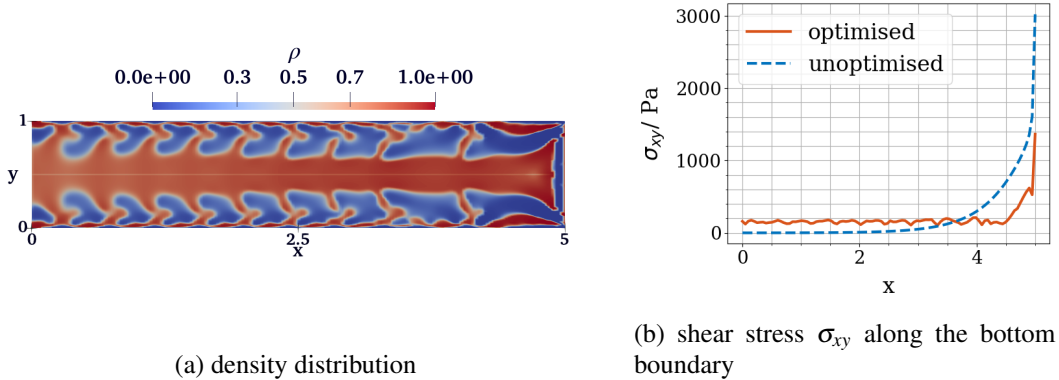


Figure 4.10: Design and stress distribution for $F = 300$ N

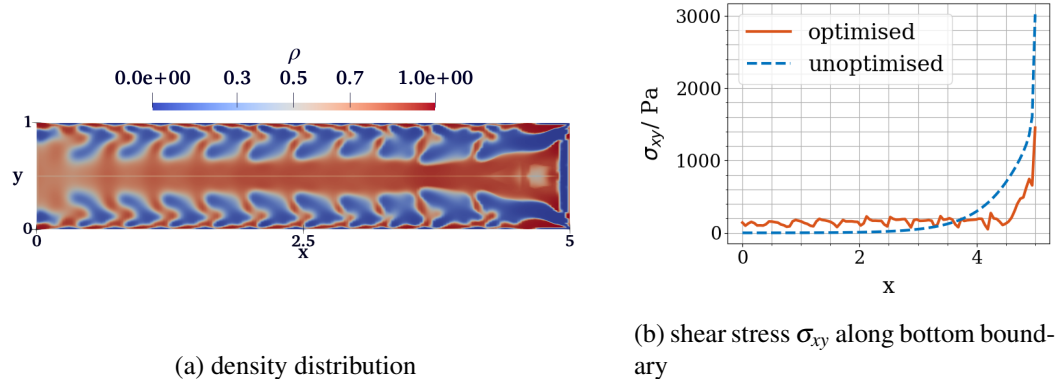


Figure 4.11: Design and stress distribution for $F = 400$ N

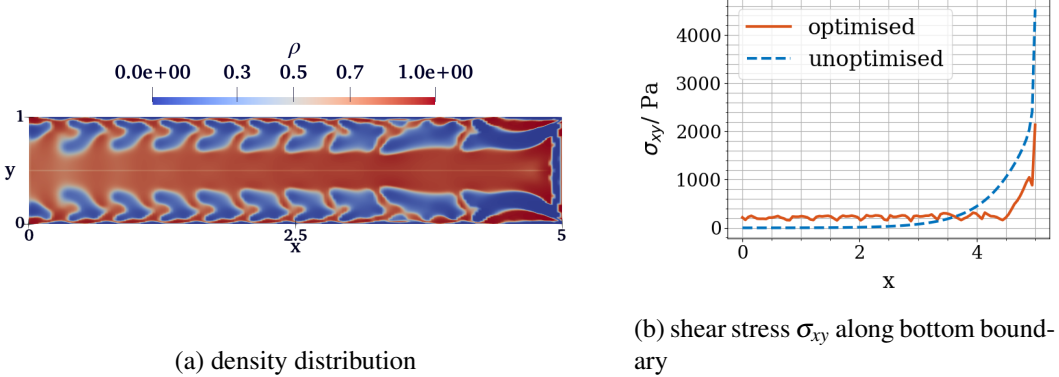


Figure 4.12: Design and stress distribution for $F = 400$ N $P = 3000$ N

It can be observed from the results of this study, that as the radial forces increase there is a thickening of the spines. This is likely due to extra material deposition to stiffen the structure and optimise it to be able to exert higher expansion forces. Spines that have larger amounts of grey densities when $F = 200$ N, tend to have smaller amounts of grey densities when the force constraint is increased. This is due to the effect of penalisation together with the constraint. The grey material is unlikely to provide the same level of stiffness as the solid material. Therefore, when higher forces are needed, the amount of grey material decreases. The thickening of spines and decrease in grey material can be observed in the spines of Figs. 4.6 and 4.10. However, this does not seem to hold for all cases of F . The amount of grey material increases in Fig. 4.11, where $F = 400$ N. The optimiser seems to be struggling to develop a structure capable of exerting such a large expansion force with the given pullout force. When the pullout force is increased for the same axial force, the structure formed is mostly discrete again. This can be observed in Fig. 4.12.

4.5 Varying a in the material deposition constraint

The parameter a controls the frequency of bands through the projection of Eq. 3.24 onto the design domain, as shown in Fig. 3.14b. This affects the distribution of spines in the design space. The number of spines and the spacing of the spines would affect the ability of the design to spread shear stresses across the boundary, as well as affect the shear stress peak seen near the head of the screw. This design aims to analyse the material distributions and stress peaks produced by varying a . To permit comparison $P = 2000$ N and $F = 200$ N for all cases discussed in this study. Results are presented for $a = 5, 10, 20$ and 30 .

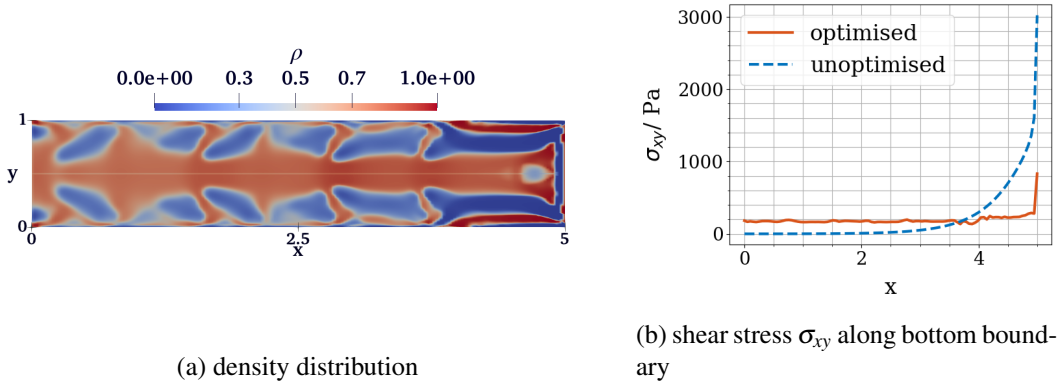
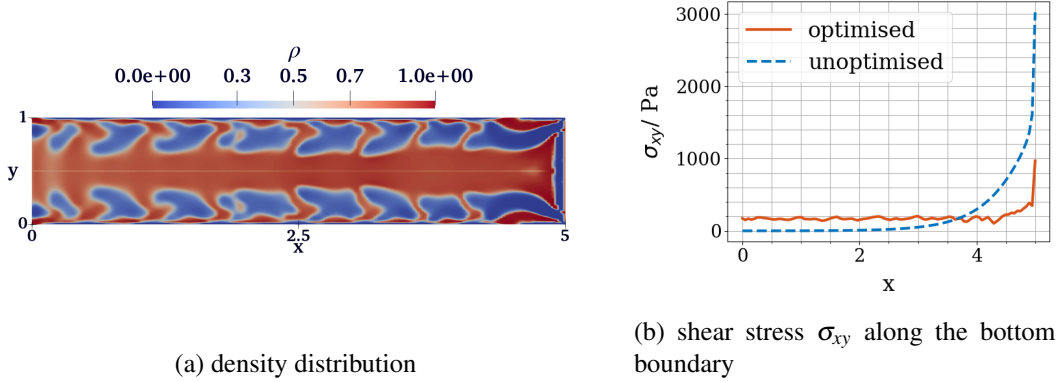
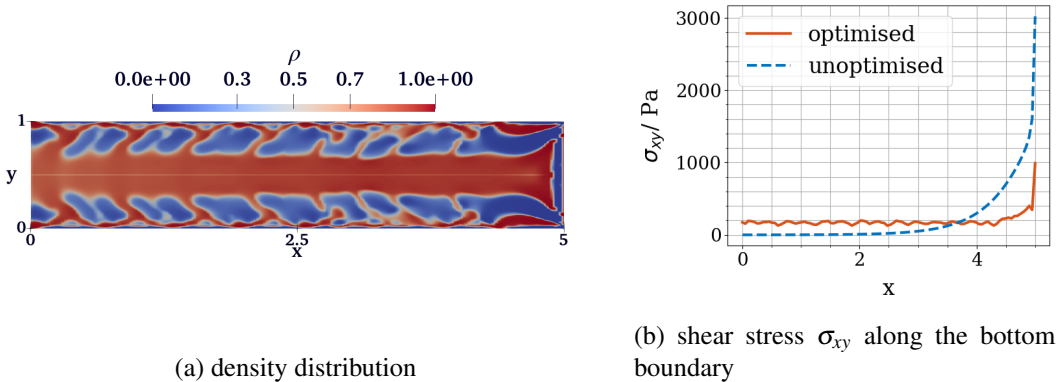
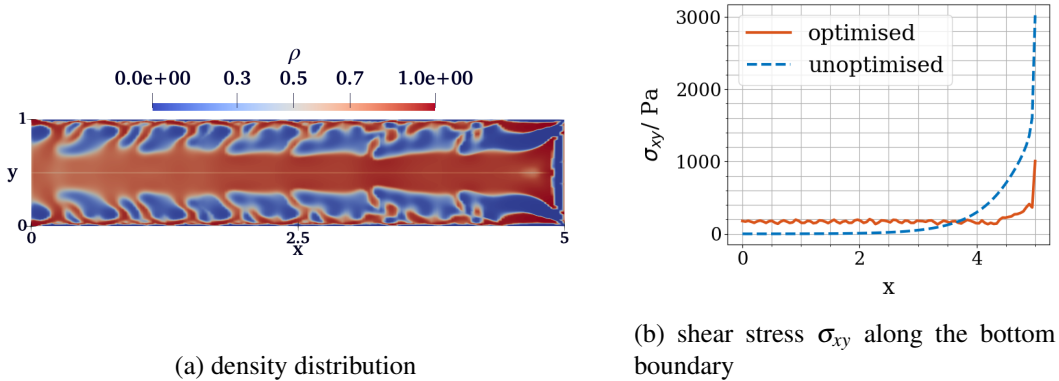


Figure 4.13: Design and stress distribution for $a = 5$

Figure 4.14: Design and stress distribution for $a = 10$ Figure 4.15: Design and stress distribution for $a = 20$ Figure 4.16: Design and stress distribution for $a = 30$

Figs. 4.13 - 4.16 present the material distributions produced by varying a . They also show the optimised stresses alongside the unoptimised stresses along the bottom boundary. Most designs created are discrete, however, the design in Fig. 4.13, shows a higher level of grey material. In general, the designs are all capable of averaging shear stresses, as the plots show the presence of shear stresses near the left-hand side boundary. The difference occurs in the shear stress peaks for each design. Fig. 4.17 shows the shear stress peak for each value of frequency, a .

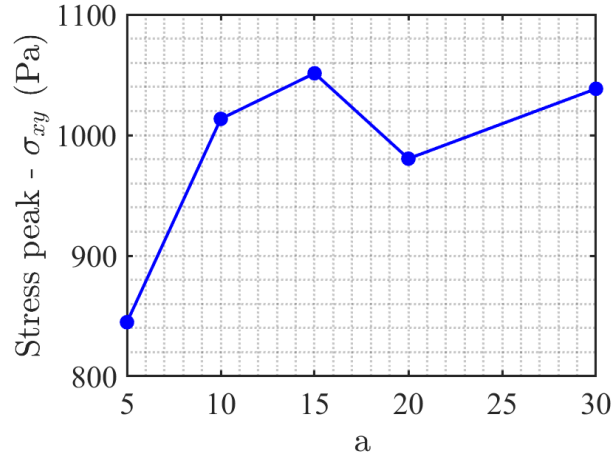


Figure 4.17: Variation of peak shear stress with frequency, a

The results show a general increase in the shear stress peak as the frequency term, a , is increased. When a is increased more bands of solid material are projected onto the design space, as shown in Fig. 3.14b. The constraint in Eq. 3.23 forces contact points between the structure and the Dirichlet boundaries. This means that the number of closely located contact points near the head of the screw increases. The shear stress concentrations near the head of the screw will then increase due to the increased number of contact points. This analysis shows that the frequency terms are important as they directly contribute towards the shear stress peaks and must be chosen carefully.

4.6 Evaluation of von Mises stresses, σ_M

Another method of screw failure is the fracture of the implant itself, and it can be brought on by high stresses in the fracture site[6]. Therefore, it is important to check for material failure in the designs created from this study. The von Mises stress field can be calculated for a given design to check for material failure. The von Mises stress is defined as

$$\mathbf{s} = \boldsymbol{\sigma} - \frac{1}{3} \text{tr}(\boldsymbol{\sigma}) \mathbf{I} \quad (4.3)$$

$$\sigma_M = \sqrt{\frac{3}{2} \mathbf{s} : \mathbf{s}}$$

The yield strength for the chosen titanium alloy is given in Tab. 2.1 and is in the range 795-895 MPa. Using Eq. 4.3, the von Mises stress field for the screw design created with a pullout force of 3000 N was evaluated. The screw design with this pullout force is presented in Fig. 4.8. The calculated von Mises stress field for $P = 3000$ N is shown in Fig. 4.18.

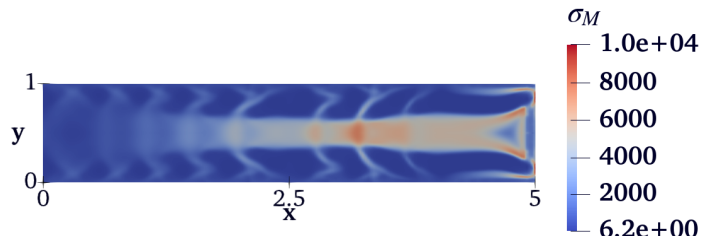


Figure 4.18: von Mises stress field for $P = 3000$ N

The maximum recorded value of the von Mises stress for the case of $P = 3000$ N is $\sigma_M = 10$ MPa. This stress value is well below the yield stress of the chosen titanium alloy. Since the von Mises stress depends on the applied forces, the other cases with lower pullout forces will also remain below the yield threshold.

4.7 Post-processing

The density distributions shown in the previous sections were mostly discrete. However, for 3D printing or clearer presentation purposes, it is necessary to perform some post-processing steps to remove any existing grey material. This process can be conducted through the use of iso-density curves[58]. This process is performed on the material distribution shown in Fig. 4.16a to showcase the effect of filtering on the final material distribution. The results of iso density filtering are shown in Fig. 4.19 for different intermediate density values.

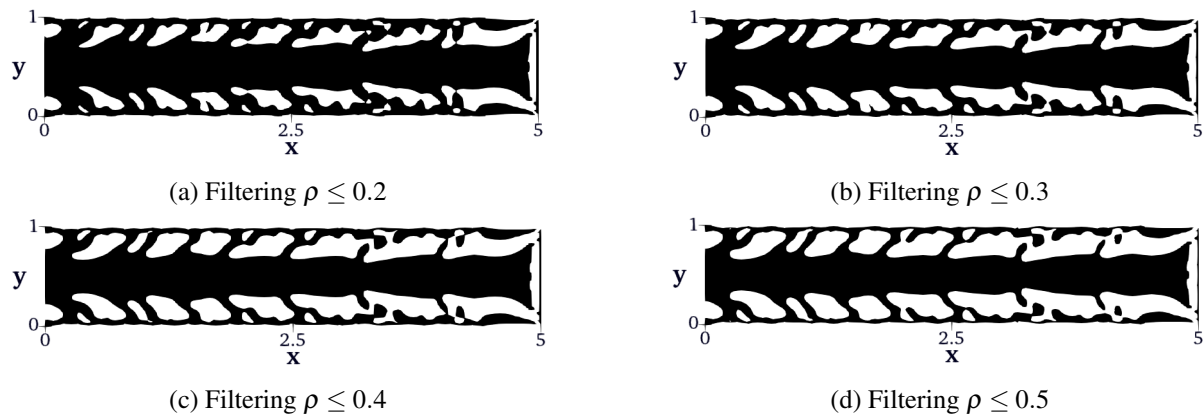


Figure 4.19: Effect of post-processing on final material distributions

These post-processed material distributions can be used for further evaluations in finite element models for verification. Smoothed and extruded material distributions can also be 3D printed.

Chapter 5

Conclusion & future work

Bone screws can fail due to stress shielding effects where the screw is much stiffer than the bone and leads to bone resorption around the implant as the bone does not receive its usual stimuli. They also fail due to screw purchase failure or in other words, failure of the bone around the screw due to high shear stresses. This is investigated through means of pullout testing and was the failure mechanism of interest for this study. Conventional bone screws and their designs have mostly been investigated in the past through experimental means. These methods permitted the investigation of screw parameters such as the pitch, major and minor diameters. Most studies found that these screw properties would affect the maximum screw purchase strength and any optimisation was done through changes to these properties. However, these studies confirm that the true reason behind screw failure in pullout is the shear stress concentrations found at the starting threads of the screw. Most screw parameters affected the volume of bone held by the threads and how well shear concentrations were passed to the bone. Changes to the screw design externally would not address the formation of the shear stress concentrations, due to the inherent nature of the problem. To mitigate the stress concentrations near the initial threads it is important to produce a structure capable of averaging shear stresses across a boundary. To perform this task topology optimisation techniques were applied in the context. Density-based methods such as SIMP are widely used and can be easily implemented with a finite element solver such as Firedrake. The first part of the report aimed at creating a simple but robust base code to perform compliance-based optimisation. After testing the code against standard test cases, it was modified to accomplish the task of optimising bone screws. A new objective function was created for the optimisation problem to perform the task of averaging stresses across the Dirichlet boundary conditions. The new objective function did not penalise grey densities naturally. This led to the application of the projection filter and the intermediate density penalisation constraint to encourage the formation of discrete designs.

Additional constraints were then added to encourage growth along the length of the screw in terms of material deposition constraints and displacement constraints. Then a new constraint was added such that the screw could exert radial forces on its boundary during pullout. This constraint would allow the optimiser to create an auxetic structure that would perform better during pullout, as seen by previous studies using NPR metamaterials in bone screws [33]. Finally, it was shown that the full domain leads to an asymmetric design, despite the symmetric nature of the problem. It was theorised that asymmetric loading conditions from the imposed constraints could lead to this problem. Therefore, a new half-domain was simulated with a symmetric boundary condition. This domain had excellent runtime and greatly improved convergence.

Finally, the designs created by the topology optimisation code were analysed by varying control parameters. This report investigated the variation of the design with pullout force P , radial force F and frequency a . This investigation highlights the ability of the new design to spread shear stresses across a boundary as seen in Figs. 4.4b - 4.8b. The new design exhibited shear stresses near the free boundary and significantly reduced peak stress compared to the unoptimised case. This investigation shows that

the objective function utilised has successfully created a structure capable of averaging shear stresses along the fixed Dirichlet boundaries.

During this investigation, it was noted that the material deposition constraint could be further investigated for its ability to decrease shear concentrations even further. Overall, the final screw designs were mostly discrete and while some intermediate densities exist, they could be removed through post-processing of the final designs.

Progression of this work would include further testing of this model and identifying other optimisation parameters such as the frequency, a . The model created in Firedrake can be easily implemented in 3D, with some minor changes to accommodate the new dimension. Future studies would investigate the change of the objective function in Eq. 3.15 to facilitate the evaluation of shear stresses in three dimensions. Due to the computational costs experienced by the model in 2D, it would be beneficial to implement multiprocessing for 3D simulations of the problem. This would not only speed up the processes but would also allow finer meshes to be used. Finally, to truly understand the design and its shortcomings it would be necessary to perform pullout tests on 3D-printed models. This would verify the performance of these screw topologies as well as provide information on the limits of the design. Future work should also investigate the 3D printing and manufacturing defects that may impact the efficiency of the structure.

Bibliography

1. Cowan PT and Kahai P. Anatomy, Bones. StatPearls Publishing, Treasure Island (FL), 2023. Available from: <http://europepmc.org/books/NBK537199>
2. Clarke B. Normal bone anatomy and physiology. Clinical journal of the American Society of Nephrology 2008; 3:S131–S139. DOI: 10.2215/CJN.04151206
3. Standring S. Functional Anatomy of the Musculoskeletal System. *Gray's Anatomy*. Ed. by Standring S. Forty Second edition. 2021 :85–126.e2. DOI: 10.1016/B978-0-7020-7705-0.00005-7
4. A. Decoster T, B. Heetderks D, J. Downey D, S. Ferries J, and Jones W. Optimizing Bone Screw Pullout Force. Journal of Orthopaedic Trauma 1990; 4:169–74
5. Yahiro MA. Comprehensive literature review: pedicle screw fixation devices. Spine 1994; 19:2274S–2278S
6. Agarwal R, Guptas V, and Singh J. Additive manufacturing-based design approaches and challenges for orthopaedic bone screws: a state-of-the-art review. Journal of the Brazilian Society of Mechanical Sciences and Engineering 2022; 44. DOI: 10.1007/s40430-021-03331-8
7. Panagiotopoulou VC, Varga P, Richards RG, Gueorguiev B, and Giannoudis PV. Late screw-related complications in locking plating of proximal humerus fractures: A systematic review. Injury 2019; 50:2176–95. DOI: 10.1016/j.injury.2019.11.002
8. Galbusera F, Volkheimer D, Reitmaier S, Berger-Roscher N, Kienle A, and Wilke HJ. Pedicle screw loosening: a clinically relevant complication? European spine journal 2015; 24:1005–16. DOI: 10.1007/s00586-015-3768-6
9. Ponnusamy KE, Iyer S, Gupta G, and Khanna AJ. Instrumentation of the osteoporotic spine: biomechanical and clinical considerations. The Spine Journal 2011; 11. Elsevier:54–63. DOI: 10.1016/j.spinee.2010.09.024
10. El Saman A, Meier S, Sander A, Kelm A, Marzi I, and Laurer H. Reduced loosening rate and loss of correction following posterior stabilization with or without PMMA augmentation of pedicle screws in vertebral fractures in the elderly. European Journal of Trauma and Emergency Surgery 2013; 39. Springer:455–60. DOI: 10.1007/s00068-013-0310-6
11. Gefen A. Optimizing the biomechanical compatibility of orthopedic screws for bone fracture fixation. Medical engineering & physics 2002; 24. Elsevier:337–47. DOI: 10.1016/S1350-4533(02)00027-9
12. Hughes AN and Jordan BA. The mechanical properties of surgical bone screws and some aspects of insertion practice. Injury 1972; 4. Elsevier:25–38. DOI: 10.1016/S0020-1383(72)80007-X
13. A Gustafson Peter P, M Veenstra Joshua M, R Bearden Cody M, and R Jastifer James M. The Effect of Pitch Variation and Diameter Variation on Screw Pullout. Foot and Ankle Specialist 2019; 12:258–63. DOI: 10.1177/1938640018789999

14. Sherman WO. OPERATIVE TREATMENT OF FRACTURES: REPORT OF FIFTY-FIVE CASES IN WHICH LANE BONE PLATES AND SCREWS WERE EMPLOYED. *Journal of the American Medical Association* 1912; LVIII:1557–61. DOI: 10.1001/jama.1912.04260050233001
15. Lešić AR, Zagorac S, Bumbaširević V, and Bumbaširević MŽ. The development of internal fixation: historical overview. *Acta chirurgica iugoslavica* 2012; 59:9–13. DOI: 10.2298/ACI1203009L
16. Kabins MB and Weinstein JN. The history of vertebral screw and pedicle screw fixation. *The Iowa orthopaedic journal* 1991; 11:127
17. Tigani D, Fosco M, Ayad RB, and Fantasia R. Orthopaedic implant materials and design. *Wear of orthopaedic implants and artificial joints. use for referencing the materials and design of bone screws in the lit review.* Elsevier, 2013 :133–77. DOI: 10.1533/9780857096128.1.133
18. Hanawa T. Overview of metals and applications. *Metals for biomedical devices.* Elsevier, 2019 :3–29. DOI: 10.1016/B978-0-08-102666-3.00001-8
19. Zindani D, Kumar K, and Davim JP. Metallic biomaterials—A review. *Mechanical Behaviour of Biomaterials* 2019. Elsevier:83–99. DOI: 10.1016/B978-0-08-102174-3.00004-8
20. Liu S and Shin YC. Additive manufacturing of Ti6Al4V alloy: A review. *Materials & Design* 2019; 164. Elsevier:264–1275. DOI: 10.1016/j.matdes.2018.107552
21. Huang YM, Huang CC, Tsai PI, Yang KY, Huang SI, Shen HH, Lai HJ, Huang SW, Chen SY, Lin FH, et al. Three-dimensional printed porous titanium screw with bioactive surface modification for bone–tendon healing: a rabbit animal model. *International journal of molecular sciences* 2020; 21:3628. DOI: 10.3390/ijms21103628
22. Yao Y, Wang L, Li J, Tian S, Zhang M, and Fan Y. A novel auxetic structure based bone screw design: Tensile mechanical characterization and pullout fixation strength evaluation. *Materials & design* 2020; 188:108424. DOI: 10.1016/j.matdes.2019.108424
23. Ernberg JJ and Asnis SE. Materials and manufacturing of orthopaedic bone screws. *Cannulated Screw Fixation: Principles and Operative Techniques.* Springer, 1996 :1–14. DOI: 10.1007/978-1-4612-2326-9_1
24. Dhandapani R, Krishnan PD, Zennifer A, Kannan V, Manigandan A, Arul MR, Jaiswal D, Subramanian A, Kumbar SG, and Sethuraman S. Additive manufacturing of biodegradable porous orthopaedic screw. *Bioactive materials* 2020; 5:458–67. DOI: 10.1016/j.bioactmat.2020.03.009
25. Standring S, Ellis H, Healy J, Johnson D, Williams A, Collins P, and Wigley C. Gray's anatomy: the anatomical basis of clinical practice. *American journal of neuroradiology* 2005; 26. Am Soc Neuroradiology:195–6108
26. Çetin A and Ali Bircan D. Experimental investigation of pull-out performance of pedicle screws at different polyurethane (PU) foam densities. *Journal of Engineering in Medicine* 2021; 235:709–16. DOI: 10.1177/09544119211002587
27. R. Chapman J, M. Harrington R, M. Lee K, A. Anderson P, F. Tencer A, and Kowalski D. Factors affecting the pullout strength of cancellous bone screws. *Journal of Biomechanical Engineering* 1996; 118:391–8. DOI: 10.1115/1.2796022
28. Weilding M, Heilemann M, Schoefelder S, and E. Heyde C. Influence of thread design on anchorage of pedicle screws in cancellous bone: an experimental and analytical analysis. *Scientific Reports* 2022; 12. DOI: 10.1038/s41598-022-11824-2
29. Kim YY, Choi WS, and Rhyu KW. Assessment of pedicle screw pullout strength based on various screw designs and bone densities—an ex vivo biomechanical study. *The Spine Journal* 2012; 12:164–8. DOI: 10.1016/j.spinee.2012.01.014

30. Feng X, Luo Z, Li Y, Yao Y, Qi W, Chen B, and Liang H. Fixation stability comparison of bone screws based on thread design: buttress thread, triangle thread, and square thread. *BMC Musculoskeletal Disorders* 2022; 23. DOI: 10.1186/S12891-022-05751-6
31. Evans M, Spencer M, Wang Q, White SH, and Cunningham JL. Design and testing of external fixator bone screws. *Journal of biomedical engineering* 1990; 12. Elsevier:457–62. DOI: 10.1016/0141-5425(90)90054-Q
32. Pothier S, Roufail R, and Malton M. Unit Cell Modelling of Auxetic Structure. *Journal of Minerals and Materials Characterization and Engineering* 2022; 10:360–9. DOI: 10.4236/jmmce.2022.104025
33. Yao Y, Wang L, Li J, Tian S, Zhang M, and Fan Y. A novel auxetic structure based bone screw design: Tensile mechanical characterization and pullout fixation strength evaluation. *Materials & design* 2020; 188. Elsevier:264–1275. DOI: 10.1016/j.matdes.2019.108424
34. Jihong ZHU, Han Z, Chuang W, Lu Z, Shangqin Y, and Zhang W. A review of topology optimization for additive manufacturing: Status and challenges. *Chinese Journal of Aeronautics* 2021; 34. Elsevier:91–110. DOI: 10.1016/j.cja.2020.09.020
35. Krog L, Tucker A, Rollema G, et al. Application of topology, sizing and shape optimization methods to optimal design of aircraft components. *Proc. 3rd Altair UK HyperWorks users conference*. 2002
36. Huang X and Xie YM. A further review of ESO type methods for topology optimization. *Structural and Multidisciplinary Optimization* 2010; 41. Springer:671–83. DOI: 10.1007/s00158-010-0487-9
37. Bendsøe MP and Kikuchi N. Generating optimal topologies in structural design using a homogenization method. *Computer methods in applied mechanics and engineering* 1988; 71:197–224. DOI: 10.1016/0045-7825(88)90086-2
38. Thillaithovan D, Murphy R, Hewson R, and Santer M. Inverse design of periodic microstructures with targeted nonlinear mechanical behaviour. *Structural Multidisciplinary Optimisation* 2024. DOI: 10.1007/s00158-024-03761-7
39. Wang F, Sigmund O, and Jensen JS. Design of materials with prescribed nonlinear properties. *Journal of the Mechanics and Physics of Solids* 2014; 69. Elsevier:156–74. DOI: 10.1016/j.jmps.2014.05.003
40. Bruns TE and Tortorelli DA. Topology optimization of non-linear elastic structures and compliant mechanisms. *Computer methods in applied mechanics and engineering* 2001; 190:3443–59. Available from: <https://www.proquest.com/dissertations-theses/topology-optimization-nonlinear-elastic/docview/275990988/se-2>
41. Bendsøe MP and Sigmund O. *Topology Optimization: Theory, Methods and Applications*. en. Springer, 2004 Feb
42. Sigmund O. A 99 line topology optimization code written in Matlab. *Structural and multidisciplinary optimization* 2001; 21:120–7. DOI: 10.1007/s001580050176
43. Andreassen E, Clausen A, Schevenels M, Lazarov BS, and Sigmund O. Efficient topology optimization in MATLAB using 88 lines of code. *Structural and Multidisciplinary Optimization* 2011; 43:1–16. DOI: 10.1007/s00158-010-0594-7
44. Bendsøe MP and Sigmund O. Material interpolation schemes in topology optimization. *Archive of applied mechanics* 1999; 69:635–54. DOI: 10.1007/s004190050248
45. Lazarov BS and Sigmund O. Filters in topology optimization based on Helmholtz-type differential equations. *International Journal for Numerical Methods in Engineering* 2011; 86:765–81. DOI: 10.1002/nme.3072

46. Bourdin B. Filters in topology optimization. *International journal for numerical methods in engineering* 2001; 50:2143–58. DOI: 10.1002/nme.116
47. Lazarov BS and Sigmund O. Sensitivity filters in topology optimisation as a solution to Helmholtz type differential equation. *8th world congress on structural and multidisciplinary optimization*. 2009
48. Jog CS and Haber RB. Stability of finite element models for distributed-parameter optimization and topology design. *Computer methods in applied mechanics and engineering* 1996; 130:203–26. DOI: 10.1016/0045-7825(95)00928-0
49. Diaz A and Sigmund O. Checkerboard patterns in layout optimization. *Structural optimization* 1995; 10:40–5. DOI: 10.1007/BF01743693
50. Wächter A and Biegler LT. On the implementation of an interior-point filter line-search algorithm for large-scale nonlinear programming. *Mathematical programming* 2006; 106. Springer:25–57. DOI: 10.1007/s10107-004-0559-y
51. Ferro RM and Pavanello R. A Simple and Efficient Structural Topology Optimization Implementation Using Open-Source Software for All Steps of the Algorithm: Modeling, Sensitivity Analysis and Optimization. *Computer Modelling in Engineering and Sciences* 2023. DOI: 10.32604/cmes.2023.026043
52. Ham DA, Kelly PHJ, Mitchell L, Cotter CJ, Kirby RC, Sagiayama K, Bouziani N, Vorderwuelbecke S, Gregory TJ, Betteridge J, Shapero DR, Nixon-Hill RW, Ward CJ, Farrell PE, Brubeck PD, Marsden I, Gibson TH, Homolya M, Sun T, McRae ATT, Luporini F, Gregory A, Lange M, Funke SW, Rathgeber F, Bercea GT, and Markall GR. Firedrake User Manual. First edition. Imperial College London et al. 2023 May. DOI: 10.25561/104839
53. Fish J and Belytschko T. A first course in finite elements. Vol. 1. Wiley New York, 2007
54. Schultz SM. An Experimental and Computational Mechanical Analysis of Bone Anchors and Substrate Interface. 2020. Available from: <https://repository.fit.edu/etd/583>
55. Xu M, Yang J, H. Lieberman I, and Haddas R. Finite element method-based study of pedicle screw–bone connection in pullout test and physiological spinal loads. *Medical Engineering and Physics* 2019; 67:11–21. DOI: 10.1016/j.medengphy.2019.03.004
56. Wang F, Lazarov BS, and Sigmund O. On projection methods, convergence and robust formulations in topology optimization. *Structural and multidisciplinary optimization* 2011; 43. Springer:767–84. DOI: 10.1007/s00158-010-0602-y
57. Borrvall T and Petersson J. Topology optimization using regularized intermediate density control. *Computer Methods in Applied Mechanics and Engineering* 2001; 190. Elsevier:4911–28. DOI: 10.1016/S0045-7825(00)00356-X
58. Sigmund O. Morphology-based black and white filters for topology optimization. *Structural and Multidisciplinary Optimization* 2007; 33:401–24. DOI: 10.1007/s00158-006-0087-x
59. Qian X. Undercut and overhang angle control in topology optimization: a density gradient based integral approach. *International Journal for Numerical Methods in Engineering* 2017; 111:247–72. DOI: 10.1002/nme.5461